


 Cite this: *RSC Adv.*, 2025, 15, 35445

# Pyrido-indole-one hybrids as potential anticancer agents against breast carcinoma: development of Ru(II)-catalyzed annulation of indole-2-carboxamides, biological screening and molecular docking studies

 Mommuleti Pradeep Kumar,<sup>a</sup> Tukki Sarkar,<sup>†</sup> Vemavarapu Durga Prasad,<sup>†a</sup> Nidhi Sharma,<sup>†bc</sup> Harish Kumar B.,<sup>b</sup> Andagulapati Sai Balaji<sup>\*bc</sup> and Bathini Nagendra Babu<sup>†ac</sup>

Breast cancer continues to pose a major worldwide health concern, characterized by its complexity and the diverse nature of its molecular subtypes. Among these, triple-negative breast cancers (TNBCs) present a formidable obstacle due to their aggressive progression and lack of targeted hormonal therapies. Molecular hybridization is a compelling strategy in drug design and development, combining distinct bioactive components to enhance potency and selectivity. Herein, we present the design and synthesis of a new series of pyrido-indole-one hybrids featuring a  $\beta$ -carboline core, by utilizing the molecular hybridization strategy, integrating indole-2-carboxamides with ynone functionalities to mitigate TNBC progression. A novel synthetic approach has been devised for synthesizing hybrid molecules, employing annulation of indole-2-carboxamides with ynones, facilitated by a Ru-complex catalyst. All the reaction conditions are meticulously optimized to yield the target hybrid molecules. Among the synthesized hybrids, **9c** exhibits strong anticancer potency against MCF-7, 4T1 and MDA-MB-231 breast carcinoma cell lines with IC<sub>50</sub> values of 4.34 ± 0.31  $\mu$ M, 3.71 ± 0.39  $\mu$ M and 0.77 ± 0.03  $\mu$ M respectively. Moreover, compound **9c** exhibits IC<sub>50</sub> values of 7.96 ± 0.04  $\mu$ M and 7.18 ± 0.32  $\mu$ M in normal HEK-293 kidney cells and BEAS-2B lung cells respectively, indicating ~10-fold preference for highly aggressive MDA-MB-231 breast cancer cells. Further analyses demonstrated that compound **9c** effectively induces cell cycle arrest in MCF-7, 4T1 and MDA-MB-231 breast cancer cells, subsequently leading to a dose-dependent increase in apoptotic cell death. In addition, compound **9c** also attenuated the formation of three-dimensional multicellular tumor spheroids (MCTSSs), indicating its potential to hinder spheroid development. The molecular docking analysis further elucidates the binding affinity of **9c** toward epidermal growth factor receptor (EGFR). As a result, the active hybrid **9c** demonstrates strong potential in engaging key cancer-related pathways, further emphasizing its significance in the advancement of next-generation anticancer therapeutics.

 Received 1st September 2025  
 Accepted 16th September 2025

DOI: 10.1039/d5ra06548h

[rsc.li/rsc-advances](http://rsc.li/rsc-advances)

## 1. Introduction

Breast cancer is a complex and diverse malignancy that arises from the uncontrolled growth of epithelial cells within breast tissue. Advancements in early diagnostic techniques and therapeutic interventions have markedly improved patient survival outcomes, however, breast cancer stands as the most commonly

diagnosed carcinoma and remains the primary cause of cancer-related fatalities among women worldwide.<sup>1,2</sup> Depending on the presence of hormone receptors such as estrogen receptor (ER), progesterone receptor (PR), and human epidermal growth factor receptor 2 (HER2), breast cancer is categorized into four distinct molecular subtypes: Luminal A, Luminal B, HER2-overexpressing, and basal-like.<sup>3</sup> Basal-like breast cancers, commonly referred to as triple-negative breast cancers (TNBCs), are defined by the absence of all three hormonal receptors, making them resistant to hormonal therapies.<sup>4</sup> These cancers are highly aggressive, linked to a poor prognosis, and exhibit a significantly higher risk of early relapse and lower survival rates compared to non-TNBC cases.<sup>5-7</sup>

<sup>a</sup>Department of Fluoro-Agrochemicals, CSIR-Indian Institute of Chemical Technology, Hyderabad-500 007, India. E-mail: bathini@iict.res.in

<sup>b</sup>Department of Applied Biology, CSIR-Indian Institute of Chemical Technology, Hyderabad-500 007, India. E-mail: balaji@iict.res.in

<sup>c</sup>Academy of Scientific and Innovative Research (AcSIR), New Delhi 110025, India

<sup>†</sup> These authors contributed equally.


Chemotherapeutic agents have long been central to the systemic treatment of breast cancer. However, their effectiveness is frequently compromised by issues such as apoptotic resistance and poor efficacy against various cancers, especially in aggressive subtypes like TNBCs.<sup>8</sup> These challenges highlight the urgent demand for advanced chemotherapeutic drugs with improved specificity and enhanced therapeutic potency. In this context, molecular hybridization serves as an effective approach to merge moieties that target distinct biological pathways, offering solutions to challenges such as drug resistance and limited efficacy against aggressive diseases.<sup>9</sup> It is an innovative drug design strategy that integrates two active pharmacophores or bioactive moieties into a single hybrid molecule.<sup>10</sup> By harnessing the complementary or synergistic actions of its components, this approach seeks to enhance the therapeutic potential of the compound.<sup>9,10</sup> The resulting hybrid molecule typically demonstrates greater efficacy, improved selectivity, and fewer side effects compared to its parent compounds.<sup>11</sup> Considering this, we aim to design and develop a novel series of pyrido-indole-one hybrids with a structurally privileged  $\beta$ -carboline core by merging biologically active indoles with yrones. Our focus on developing hybrids with a  $\beta$ -carboline core stems from their recognition as a key structural motif in medicinal chemistry, widely recognized for their extensive range of biological activities, with a particular emphasis on their remarkable anticancer potential.<sup>12</sup> The  $\beta$ -carboline alkaloids are a notable class of heterocyclic compounds distinguished by their planar tricyclic pyrido-[3,4-*b*] indole ring structure.<sup>13</sup> This indole-derived alkaloid framework demonstrates cytotoxic effects against a variety of cancer cell lines through mechanisms like DNA intercalation, topoisomerase inhibition, and regulation of signaling pathways governing cell growth and programmed cell death.<sup>12,14</sup> Its adaptability supports the creation of

derivatives with improved selectivity and effectiveness, positioning it as an excellent foundation for developing potent anticancer therapeutics.<sup>15</sup> For instance, the bioactive alkaloids, including annomontine, harmine, harman, and harmaline, belong to the  $\beta$ -carboline class and are well-known for their diverse biological activities (Fig. 1A).<sup>14</sup> Very recently, Dang *et al.* synthesized a series of  $\beta$ -carboline-bisindole hybrid compounds that exhibited remarkable anticancer properties. These hybrids showed significant efficacy against three prevalent cancer cell lines: MCF-7 (breast cancer), SK-LU-1 (lung cancer), and HepG2 (liver cancer). The results emphasized the potential and the therapeutic relevance of  $\beta$ -carboline and bisindole scaffolds in treating various forms of cancer.<sup>16</sup> Kamal *et al.* reported a series of  $\beta$ -carboline-benzimidazole conjugates exhibiting potential cytotoxic effects and promising DNA topoisomerase-I inhibition. These conjugates exhibit the ability to photocleave DNA by generating singlet oxygen species under UV light.<sup>17</sup> Our group has also developed novel strategies to construct bioactive alkaloids/heterocyclic motifs and reported a unique set of  $\beta$ -carboline-linked aryl sulfonyl piperazine congeners with notable anticancer potential. The lead compounds demonstrated significant efficacy against human osteosarcoma cells, showcasing their promise as potential therapeutic agents.<sup>18,19</sup> These findings underline the importance of  $\beta$ -carboline frameworks in developing novel anticancer molecules and highlight their relevance in targeted cancer therapies.

Indoles are intriguing organic molecules recognized for their diverse biological functions. Their structure, composed of a fused benzene and pyrrole ring system, underpins their significant roles in various biological processes.<sup>20</sup> Indoles demonstrate immense potential in therapeutic applications by providing a spectrum of biological effects such as anti-inflammatory, antioxidant, anticancer, antimicrobial, and antiviral properties.<sup>21</sup>

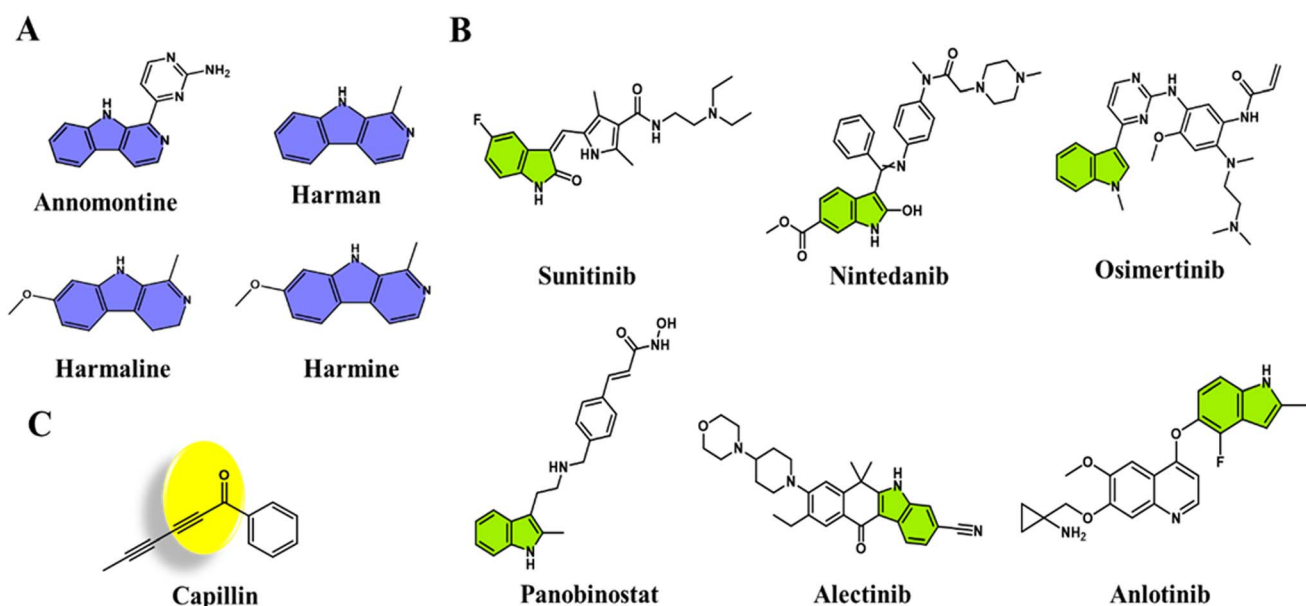


Fig. 1 (A) Chemical structures of a few bioactive  $\beta$ -carbolines. (B) Chemical structures of the FDA-approved indole-based anticancer agents. (C) A naturally occurring ynone.



These compounds interact intricately with enzymes, receptors, and signaling pathways, positioning them as crucial components in the advancement of innovative medical treatments.<sup>22</sup> Indole-based compounds effectively hinder cancer cell proliferation by disrupting cell cycle processes and triggering apoptosis (programmed cell death), showcasing their efficacy across various cancer types.<sup>23</sup> Interestingly, indole alkaloids, such as vincristine and vinblastine (vinca alkaloids), derived from natural sources, effectively engage regulated cell death pathways like apoptosis, autophagy, and ferroptosis, playing a vital role in managing tumor growth and progression.<sup>24,25</sup> It is noteworthy to mention that, Sunitinib, Nintedanib, Osimertinib, Panobinostat, Alectinib, and Anlotinib are the indole-based anticancer agents that received FDA's approval for clinical application (Fig. 1B).<sup>26</sup> Likewise, indole amides, bearing the indole core, also possess significant biological importance, owing to their wide-ranging pharmacological activities and adaptable structural framework.<sup>27</sup> They show significant potential in cancer therapy by modulating essential cellular mechanisms, including apoptosis induction, DNA intercalation, and enzyme inhibition.<sup>28</sup> Their capacity to engage with diverse biological targets underscores their importance in anticancer drug development. Additionally, the indole core acts as a flexible framework for designing numerous derivatives, enabling the production of compounds tailored to specific therapeutic needs.<sup>28,29</sup>

Ynonees often play a key role in the synthesis of a wide range of biologically active molecules and are instrumental in the development of several therapeutics, including anticancer agents, antimicrobial compounds, and anti-inflammatory drugs. Capillin, a naturally occurring compound and a primary component of *Artemisia capillaris* Thunb. flower essential oil, exemplifies a biologically active  $\alpha,\beta$ -ynone with

significant therapeutic activities, including anticancer, antimicrobial, antibacterial and antifungal properties (Fig. 1C).<sup>30</sup> Interestingly, ynonees' ability to undergo diverse chemical transformations makes them highly valuable in medicinal chemistry and pharmaceutical research.<sup>31,32</sup> Certain ynone derivatives function as enzyme inhibitors, proving instrumental in targeting disease-specific biological pathways.<sup>32</sup>

Given the significant biological relevance of indoles and ynonees, our objective is to synthesize molecular hybrids that feature an active  $\beta$ -carboline core for enhanced functionality. In this work, we detail the design, synthesis, and evaluation of the anticancer potential of a series of pyrido-indole-one hybrids with structurally privileged  $\beta$ -carboline core, developed through the integration of biologically active indole amides with ynonees using Ru-complex catalyzed annulation reaction. The notable finding includes: (i) development of convenient synthetic methodology for the preparation of molecular hybrids with careful optimization of reaction conditions, ensuring versatility and reproducibility, (ii) comprehensive characterization utilizing different physico-chemical techniques such as <sup>1</sup>H NMR, <sup>13</sup>C NMR, <sup>19</sup>F NMR spectroscopy, high resolution mass spectrometry, (HRMS) and single-crystal X-ray diffraction, to confirm the precise molecular structures, (iii) demonstration of significant anticancer activity against breast cancer cells, with a strong focus on the aggressive triple-negative breast cancer cell lines, (iv) elevated apoptosis with reduced expression of anti-apoptotic markers, (v) ability to attenuate three-dimensional multicellular tumor spheroids (MCTSs), (vi) molecular docking studies revealing affinity and potential inhibitory effects on the epidermal growth factor receptor (EGFR), yielding important information on their mechanism of action. The strategic framework guiding the hybrid design is depicted in Fig. 2.

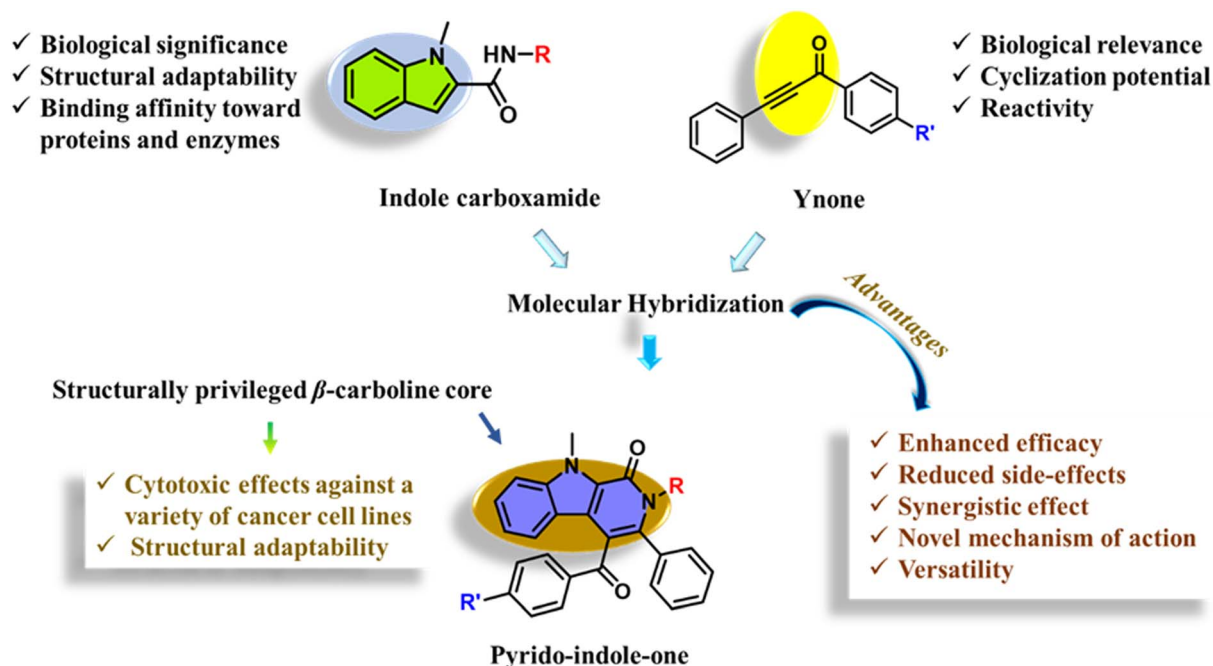


Fig. 2 Design rationale and significance of the synthesized hybrid.

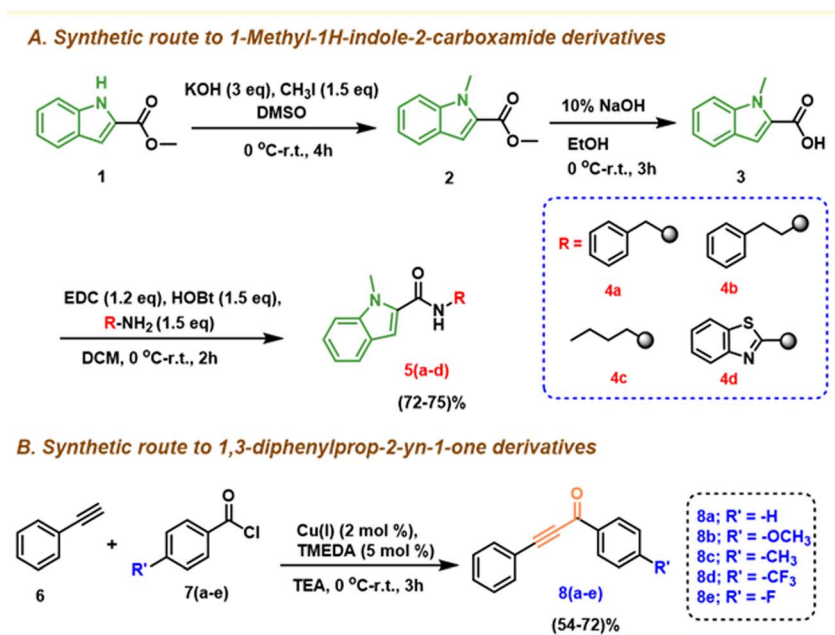


## 2. Results and discussion

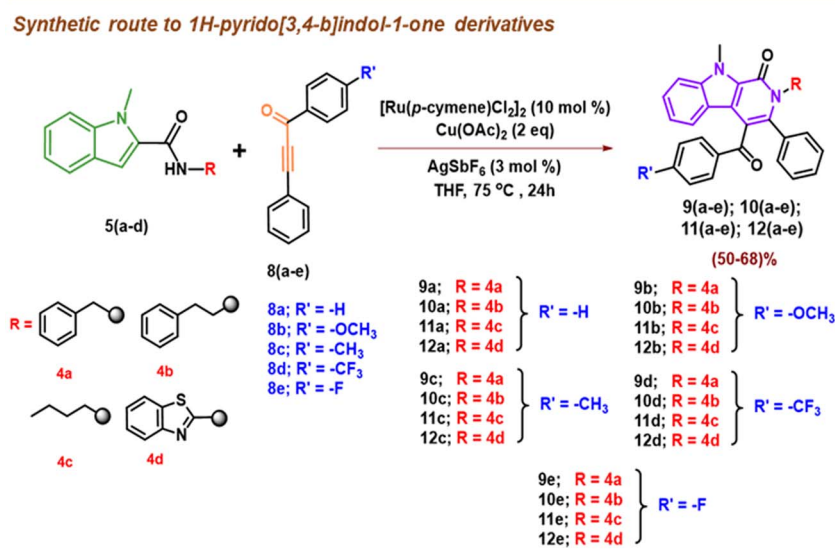
### 2.1 Chemistry

The 1*H*-pyrido[3,4-*b*]indol-1-one hybrids, [9(a-e), 10(a-e), 11(a-e) and 12(a-e)], were designed and synthesized using a convenient, novel and general synthetic approach, *via* an annulation reaction involving the indole amides 5(a-d), and ynones 8(a-e), in anhydrous tetrahydrofuran (THF), with dichloro(*p*-cymene) ruthenium(II) dimer as the catalyst, and copper(II) acetate and silver hexafluoroantimonate as additives, as outlined in Scheme

2. Reaction conditions were meticulously optimized by screening various solvents, catalyst, and additives (Table S1). The key intermediates, 5(a-d), were prepared *via* amidation of 1-methyl-1*H*-indole-2-carboxylic acid with respective amines (Scheme 1A), in the presence of 1-ethyl-3-(3-dimethylaminopropyl)carbodiimide hydrochloride (EDC·HCl) and anhydrous 1-hydroxybenzotriazole (HOBT), under inert conditions in dichloromethane (DCM), following a literature-reported method (Scheme 1A).<sup>33</sup> The ynones 8(a-e) were synthesized through coupling reaction between phenyl



Scheme 1 (A) Synthesis of 1-methyl-1*H*-indole-2-carboxamide derivatives 5(a-d). (B) Synthesis of 1,3-diphenylprop-2-yn-1-one derivatives 8(a-e).



Scheme 2 Synthesis of 1*H*-pyrido[3,4-*b*]indol-1-one derivatives 9(a-e); 10(a-e); 11(a-e) and 12(a-e).



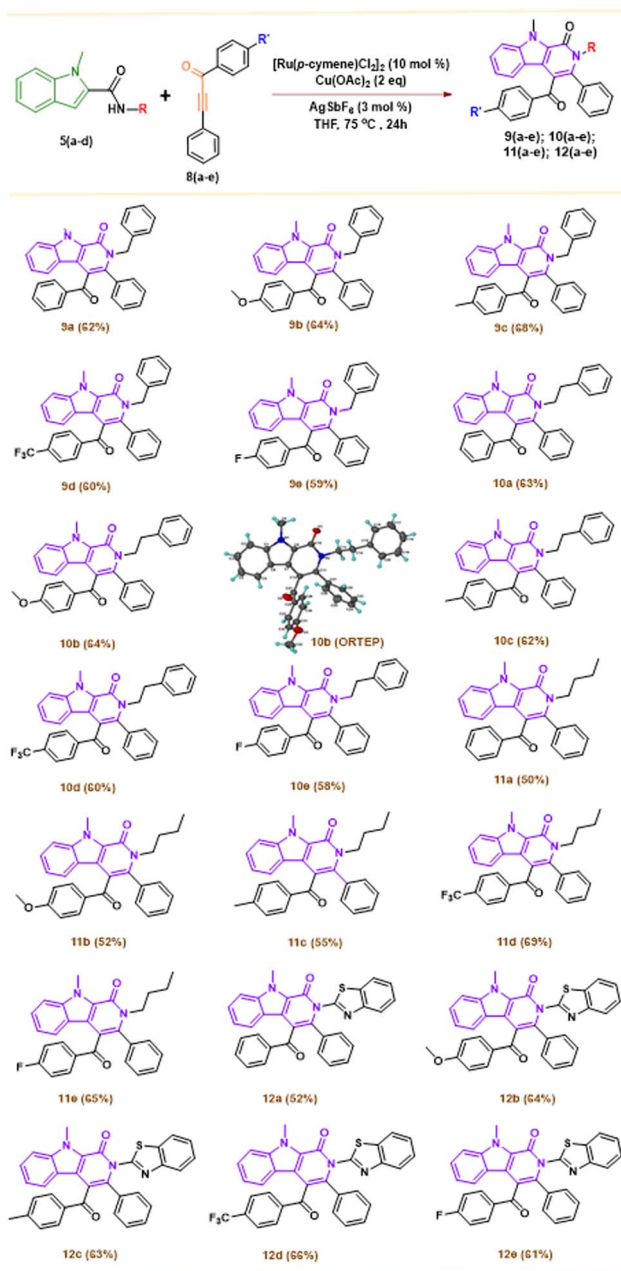


Fig. 3 Chemical representation of the synthesized hybrids [9(a–e), 10(a–e), 11(a–e) and 12(a–e)] and ORTEP diagram of **10b** with the atom-numbering. Displacement ellipsoids are drawn at the 30% probability level and H atoms are shown as small spheres of arbitrary radius. Isolated yields are mentioned in parenthesis.

acetylene and substituted benzoyl chlorides **7(a–e)**, utilizing copper iodide (CuI), *N,N,N',N'*-tetramethylethylenediamine (TMEDA), and trimethylamine (TEA) under nitrogen atmosphere, following a literature reported method with minor modification (Scheme 1B).<sup>34</sup> Final hybrids, 1*H*-pyrido[3,4-*b*]indol-1-one derivatives, were obtained *via* an annulation reaction involving the indole amides **5(a–d)**, and ynones **8(a–e)**, in anhydrous tetrahydrofuran, with dichloro(*p*-cymene)ruthenium(II) dimer as the catalyst, and copper(II) acetate and silver hexafluoroantimonate as additives (Scheme 2). The resulting

hybrid molecules, [9(a–e), 10(a–e), 11(a–e) and 12(a–e)], were purified by column chromatography and obtained in moderate to good yields. It is noteworthy to mention; this reaction did not yield the desired product with free N–H containing indole amide. The identity of the synthesized compounds was confirmed using <sup>1</sup>H NMR, <sup>13</sup>C NMR, <sup>19</sup>F NMR spectroscopy, high resolution mass spectrometry (HRMS) (Fig. S1–S86). To obtain structural insights, compound **10b** was crystallized (CCDC deposition number 2446994) and its X-ray single-crystal structure (solid-state) was determined. The chemical representation, alongside the ORTEP depiction of **10b** at a 30% thermal probability is given in Fig. 3.

The distinct crystals of compound **10b** formed in 1:3 ethanol/DCM solution, adopting the *Pbca* space group, characteristic of the orthorhombic crystal system. Following comprehensive characterization, the synthesized hybrids were screened to evaluate their anticancer potential. Additionally, molecular docking studies were conducted to deepen the understanding of their binding affinity toward EGFR. A general schematic outline illustrating the present study is given in Fig. 4.

## 2.2 Biology

**2.2.1 Cytotoxicity studies.** The synthesized 1*H*-pyrido[3,4-*b*]indol-1-one hybrids were screened for their cytotoxicity against three cancerous breast cell lines, namely, MCF-7 (estrogen receptor (ER) positive and progesterone receptor (PR) positive), 4T1 (Mouse TNBCs), and MDA-MB-231 (Human TNBCs) breast cancer cells. The percentage of average cell death was determined, at a concentration of 25 μM using sulforhodamine B (SRB) cytotoxicity assay. The results, as summarized in Table 1, indicated that compound **9c** exhibited the highest cytotoxic effects, with average cell death percentages of 75.14 ± 0.02%, 72.34 ± 0.04%, and 94.73 ± 1.10% in MCF-7, 4T1, and MDA-MB-231 cells, respectively. In contrast, other compounds demonstrated significantly lower cytotoxicity, ranging from 1.67% to 60.49%, indicating varying degrees of activity. Interestingly, the compound **9c** exhibited potent cytotoxic activity against the highly aggressive MDA-MB-231 and 4T1 triple-negative breast cells (TNBCs). Further, the IC<sub>50</sub> values of the most active compound, **9c**, were determined in MCF-7, 4T1 and MDA-MB-231 cancer cell lines (Table 2), as well as in HEK-293 and BEAS-2B normal cells. In MCF-7 and 4T1 cells, **9c** exhibited IC<sub>50</sub> values of 4.34 ± 0.31 μM and 3.71 ± 0.39 μM, while in MDA-MB-231 cells the IC<sub>50</sub> value was 0.77 ± 0.03 μM, suggesting potent cytotoxicity against these breast cancer cells. In comparison, compound **9c** exhibited IC<sub>50</sub> values of 7.96 ± 0.04 μM in HEK-293 kidney cells and 7.18 ± 0.32 μM in BEAS-2B lung cells, demonstrating a pronounced ~10-fold selectivity for the highly aggressive MDA-MB-231 breast cancer cells. Consequently, compound **9c** showed strong cytotoxic effects on breast cancer cell lines, with notable potency against MDA-MB-231 cells, while maintaining a desirable selectivity profile, highlighting its potential as a promising anticancer agent for further investigation.

**2.2.2 Structure–activity relationship (SAR).** We undertook a systematic exploration of amine variants, spanning from



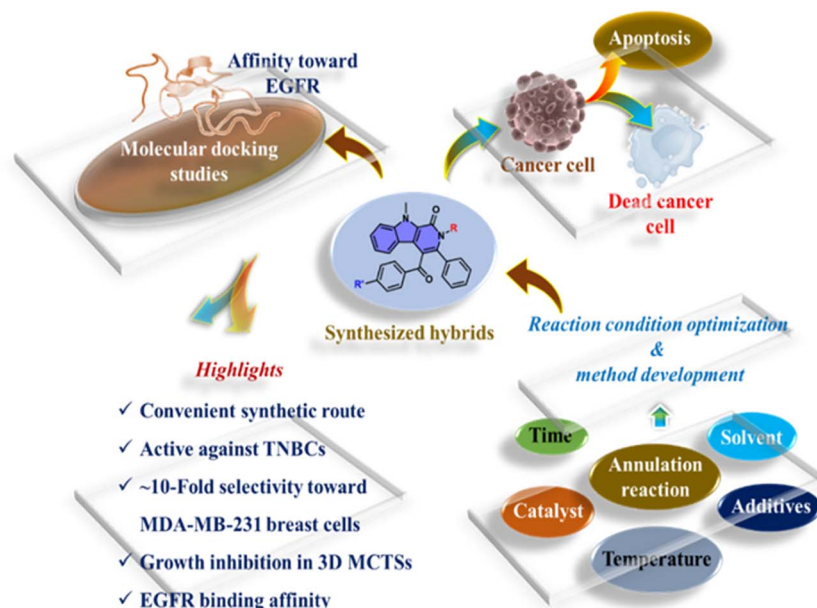


Fig. 4 A schematic overview of the current study.

**Table 1** The percentage of average cell death induced by the synthesized hybrids [9(a–e), 10(a–e), 11(a–e) and 12(a–e)] at 25  $\mu\text{M}$  as determined from the SRB assay<sup>a</sup>

Average cell death (%)			
Compound	MCF-7	4T1	MDA-MB-231
9a	9.16 $\pm$ 2.08	47.78 $\pm$ 3.32	32.82 $\pm$ 3.16
9b	18.31 $\pm$ 3.05	39.75 $\pm$ 4.02	20.18 $\pm$ 2.16
9c	<b>75.14 <math>\pm</math> 4.02</b>	<b>72.34 <math>\pm</math> 4.04</b>	<b>94.73 <math>\pm</math> 1.10</b>
9d	14.19 $\pm$ 1.03	15.47 $\pm$ 2.15	11.28 $\pm$ 0.53
9e	2.00 $\pm$ 0.52	32.23 $\pm$ 4.11	7.54 $\pm$ 0.71
10a	1.67 $\pm$ 0.30	46.56 $\pm$ 2.18	3.66 $\pm$ 0.31
10b	10.07 $\pm$ 2.20	49.92 $\pm$ 3.23	2.64 $\pm$ 0.70
10c	26.23 $\pm$ 4.15	60.49 $\pm$ 3.07	15.64 $\pm$ 1.15
10d	9.32 $\pm$ 1.00	21.97 $\pm$ 2.05	11.53 $\pm$ 0.95
10e	8.92 $\pm$ 0.80	13.54 $\pm$ 1.16	4.00 $\pm$ 0.41
11a	-nd-	-nd-	36.63 $\pm$ 3.2
11b	-nd-	-nd-	30.26 $\pm$ 1.2
11c	-nd-	-nd-	31.16 $\pm$ 1.6
11d	-nd-	-nd-	14.67 $\pm$ 2.9
11e	-nd-	-nd-	31.81 $\pm$ 1.8
12a	-nd-	-nd-	26.94 $\pm$ 2.6
12b	-nd-	-nd-	4.08 $\pm$ 1.1
12c	-nd-	-nd-	31.27 $\pm$ 4.0
12d	-nd-	-nd-	24.54 $\pm$ 2.7
12e	-nd-	-nd-	34.85 $\pm$ 1.7
Doxorubicin (at 5 $\mu\text{M}$ )	85 $\pm$ 5.3	-nd-	80 $\pm$ 3.3
Cisplatin (at 100 $\mu\text{M}$ )	80 $\pm$ 6.2	-nd-	75 $\pm$ 4.3

<sup>a</sup> -nd-: not done.

aliphatic [4(a–c)] to heteroaromatic (4d) moieties. To elucidate the structure–activity relationship (SAR) of the synthesized hybrids, five substituents (-H, -CH<sub>3</sub>, -CF<sub>3</sub>, -OMe, -F) were strategically selected to represent a spectrum of electronic and steric properties, encompassing electron-donating, electron-

**Table 2** IC<sub>50</sub> values (expressed in  $\mu\text{M}$  units) of the active hybrid 9c in different breast cancer cell lines as determined from the SRB assay<sup>a</sup>

Cell lines	IC <sub>50</sub> value of 9c
MCF-7	4.34 $\pm$ 0.31
4T1	3.71 $\pm$ 0.39
MDA-MB-231	<b>0.77 <math>\pm</math> 0.03</b>

<sup>a</sup> IC<sub>50</sub> value: 50% inhibitory concentration after 48 h of drug treatment. MCF-7: human breast adenocarcinoma; 4T1: murine triple-negative breast cancer cell, MDA-MB-231: human triple-negative breast cancer cell. Data are presented as mean  $\pm$  SD ( $n = 3$ ).

withdrawing, and neutral groups. Intriguingly, the methyl-substituted analogue 9c, with a single methylene spacer exhibited remarkable anticancer potential, in stark contrast to other structurally modified hybrids that failed to elicit significant activity. Even elongation of the alkyl chain, often a strategy to enhance lipophilicity and cellular uptake proved ineffective in improving therapeutic efficacy. The observed bioactivity of the hybrid 9c could be due to the “Magic Methyl” effect, wherein the -CH<sub>3</sub> group enhances potency by modulating molecular conformation, strengthening hydrophobic interactions, and improving lipophilicity, thereby facilitating membrane permeability and target engagement.<sup>35–37</sup> Given its compelling IC<sub>50</sub> profile against MDA-MB-231 monolayer cells, hybrid 9c was selected for expanded biological investigation.

**2.2.3 Cell cycle analysis.** Flow cytometry analysis was carried out using propidium iodide (PI) staining to assess how compound 9c influences the progression of the cell cycle. Fig. 5A and B illustrate the cell cycle profiles of MCF-7 and 4T1 cells treated with doxorubicin (0.5  $\mu\text{M}$ ) and varying concentrations of compound 9c (2  $\mu\text{M}$ , 4  $\mu\text{M}$ , and 6  $\mu\text{M}$ ). In control MCF-7 cells, the majority of the population was observed in the G1



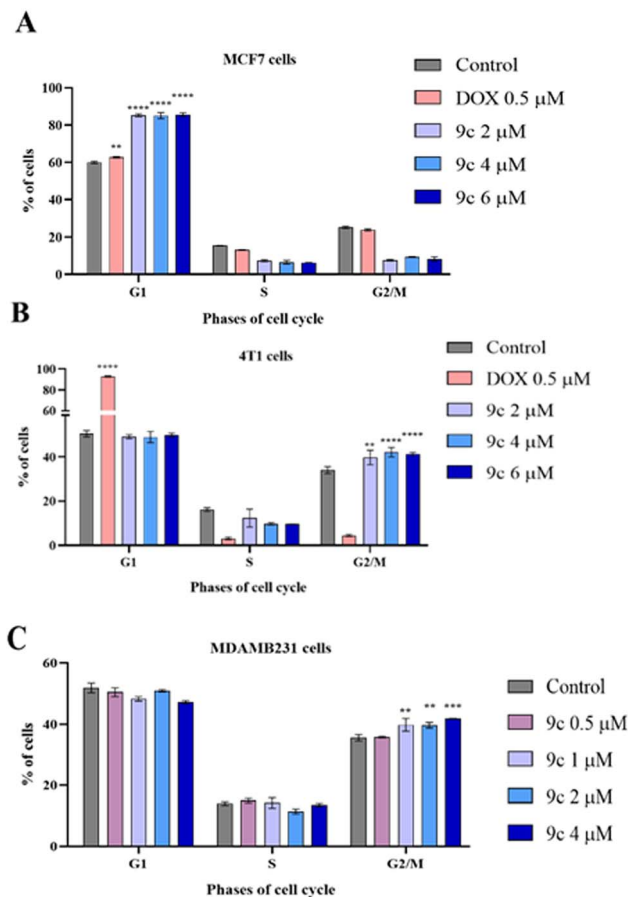


Fig. 5 Cell cycle analysis of MCF-7 cells (in A), 4T1 cells (in B) and MDA-MB-231 cells (in C) treated with **9c** in different concentrations.

phase (59.9%), with a smaller proportion in the S (15.4%) and G2/M (25.1%) phases. A concurrent decrease in cells occupying the S and G2/M phases was observed. At 6  $\mu\text{M}$ , **9c** treatment maintained a high G1 population (85.6%), confirming the compound's ability to induce G1 phase arrest in MCF-7 cells (Fig. 5A).

This was accompanied by a corresponding reduction in the S and G2/M phases aligning with standard DOX treatment. Further, flow cytometry analysis was also carried out in 4T1 cells to investigate the influence of **9c** on the cell cycle progression. In untreated control cells, the G1 phase population was 50.5%, with 16.1% and 32.5% of cells in the S and G2/M phases, respectively. Treatment with 6  $\mu\text{M}$  **9c** led to 50.1% cells in G1 phase while increasing the G2/M population to 41.1% showing G2/M arrest in 4T1 cells (Fig. 5B).

Alongside, MDA-MB-231 cells were also treated with varying concentrations of compound **9c** (0.5  $\mu\text{M}$ , 1  $\mu\text{M}$ , 2  $\mu\text{M}$ , and 4  $\mu\text{M}$ ) and subjected to flow cytometry analysis to investigate the effect of **9c** on the cell cycle progression. In MDA-MB-231 control cells, the G1 phase population was 53%, with 13.4% and 34.8% of cells in the S and G2/M phases, respectively. Treatment with 4  $\mu\text{M}$  **9c** led to 46.9% cells in G1 phase while increasing the G2/M population to 41.9% showing G2/M arrest in MDA-MB-231 cells

(Fig. 5C). Thus, it has been found that **9c** causes cell cycle arrest in MCF-7, 4T1, and MDA-MB-231 cells.

**2.2.4 Determination of apoptosis by annexin V-FITC/PI assay.** Apoptosis is a fundamental pathway driving cell death. The annexin V-FITC/PI assay serves as a technique for evaluating how effectively a compound triggers apoptosis in cells.

This assay helps distinguish between live cells, early and late apoptotic cells, as well as necrotic cells. The protein annexin V interacts with phosphatidylserine (PS) in a calcium-dependent manner. In healthy cells, PS is typically confined to the inner layer of the plasma membrane. However, during early apoptosis, this membrane symmetry is disrupted, causing PS to move to the outer leaflet. Fluorochrome-labeled annexin V enables the identification of apoptotic cells. However, annexin V binding alone cannot distinguish between necrotic and apoptotic cells. The addition of propidium iodide (PI) helps resolve this issue as early apoptotic cells resist PI entry, whereas both late apoptotic and necrotic cells allow the dye to infiltrate the nucleus and bind to DNA, resulting in positive staining. To investigate if the cytotoxic effects of **9c** were linked to apoptosis, annexin V-FITC/propidium iodide (PI) flow cytometry analysis was conducted on MCF-7 and 4T1 cells. In MCF-7 control cells, a low percentage of apoptosis was detected, with 2.3% early apoptotic cells and a total apoptotic population (early + late) of 4.1%. Treatment with **9c** induced a dose-dependent increase in apoptosis.

Specifically, early apoptosis increased to 7.2%, 8.05%, and 9.9% with 2  $\mu\text{M}$ , 4  $\mu\text{M}$ , and 6  $\mu\text{M}$  of **9c**, respectively. Correspondingly, the total apoptotic population rose to 11.3%, 14.1%, and 16.5%, confirming the pro-apoptotic potential of **9c**

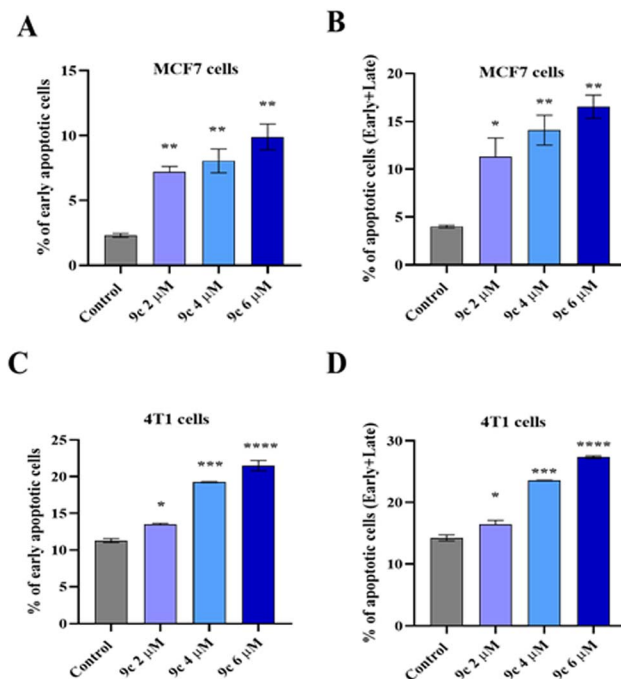


Fig. 6 Dose-dependent apoptotic cell death induced by **9c** in MCF-7 (in A and B) and 4T1 cells (in C and D); \* $p < 0.05$ , \*\* $p < 0.01$ , \*\*\* $p < 0.001$ , \*\*\*\* $p < 0.0001$ .



in MCF-7 cells (Fig. 6A and B). A similar trend was observed in 4T1 cells (Fig. 6C and D). In untreated control 4T1 cells, early apoptosis was 11.1%, with a total apoptotic percentage of 13.9%. Exposure to different concentrations of **9c** (2  $\mu\text{M}$ , 4  $\mu\text{M}$  and 6  $\mu\text{M}$ ) led to a marked, dose-dependent increase in early apoptosis (13.5%, 19.2%, and 22%) and total apoptosis (16.5%, 23.5%, and 27.2%). The observed outcomes indicate that **9c** induces apoptosis in MCF-7 and 4T1 cells in a dose-dependent manner, thereby playing a significant role in its anticancer activity.

**2.2.5 Effect of 9c on anti-apoptotic markers.** BCL-2 and Survivin are the key anti-apoptotic markers which plays a major role in progression of cancer. Over-expression of BCL-2 has been associated with enhanced cellular invasion and migration in breast cancer. As a prognostic biomarker, BCL-2 represents a promising therapeutic target, and its inhibition may offer an effective strategy for the treatment of breast cancer.<sup>38</sup> Drug resistance in TNBCs is commonly linked to the upregulation of

specific anti-apoptotic proteins within the BCL-2 family, particularly BCL-2, MCL-1, and BCL-XL.<sup>39</sup> Similarly, Survivin expression was low in hormone-positive cancers compared to TNBCs and Survivin acts directly to inactivate the apoptosis cascade and acts prognostic marker for breast cancer.<sup>40</sup> In this study, we evaluated the impact of compound **9c** on the expression of BCL-2 and Survivin in MDA-MB-231 cells. The results demonstrated that treatment with **9c** significantly down-regulated the expression of both BCL-2 and Survivin (Fig. 7). Similarly, doxorubicin treatment also markedly reduced the levels of these proteins. Collectively, these findings suggest that compound **9c** may inhibit cancer progression by suppressing the expression of key anti-apoptotic markers BCL-2 and Survivin.

**2.2.6 3D spheroid formation assay.** Many anticancer agents that perform well in 2D cell cultures often fail *in vivo* due to the limitations of monolayer systems. Multicellular tumor spheroids (MCTSS), however, offer a more realistic tumor model, replicating key features such as cellular diversity, spatial growth patterns, necrotic core formation, peripheral proliferation, and extracellular matrix production.<sup>41</sup> To evaluate the effect of compound **9c** on tumorigenic potential, we employed the methylcellulose-based sphere formation assay in MDA-MB-231 cells, a surrogate for *in vivo* tumor formation.<sup>42</sup> Untreated MDA-MB-231 cells generated well-defined spheres ( $\geq 20$  cells per sphere) within 8 days. In contrast, treatment with doxorubicin or **9c** completely abrogated sphere formation. Furthermore, **9c** reduced the number of spheres in a dose-dependent manner, exhibiting potency comparable to doxorubicin (Fig. 8). These findings indicate that **9c** effectively suppresses sphere formation, suggesting its potential as a lead candidate for translational development in breast cancer therapy.

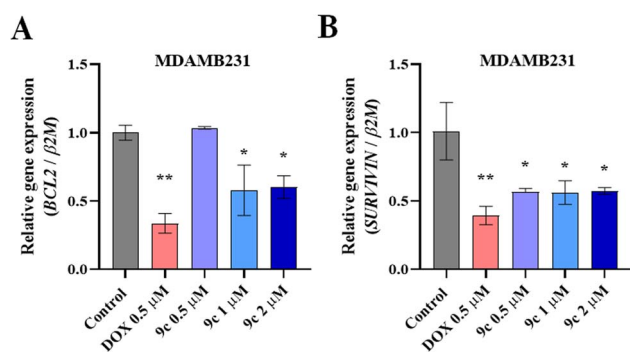


Fig. 7 Gene expression analysis for BCL2 (A) and Survivin (B) in MDA-MB-231 cells.

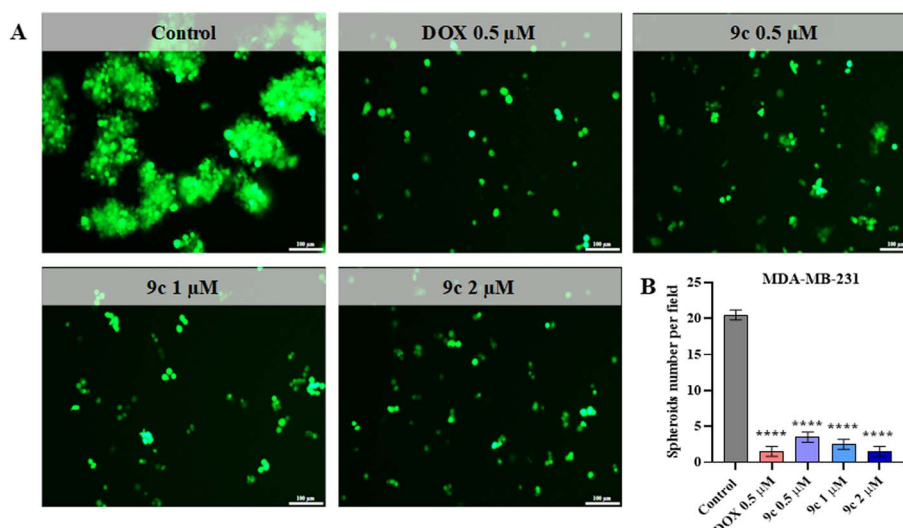
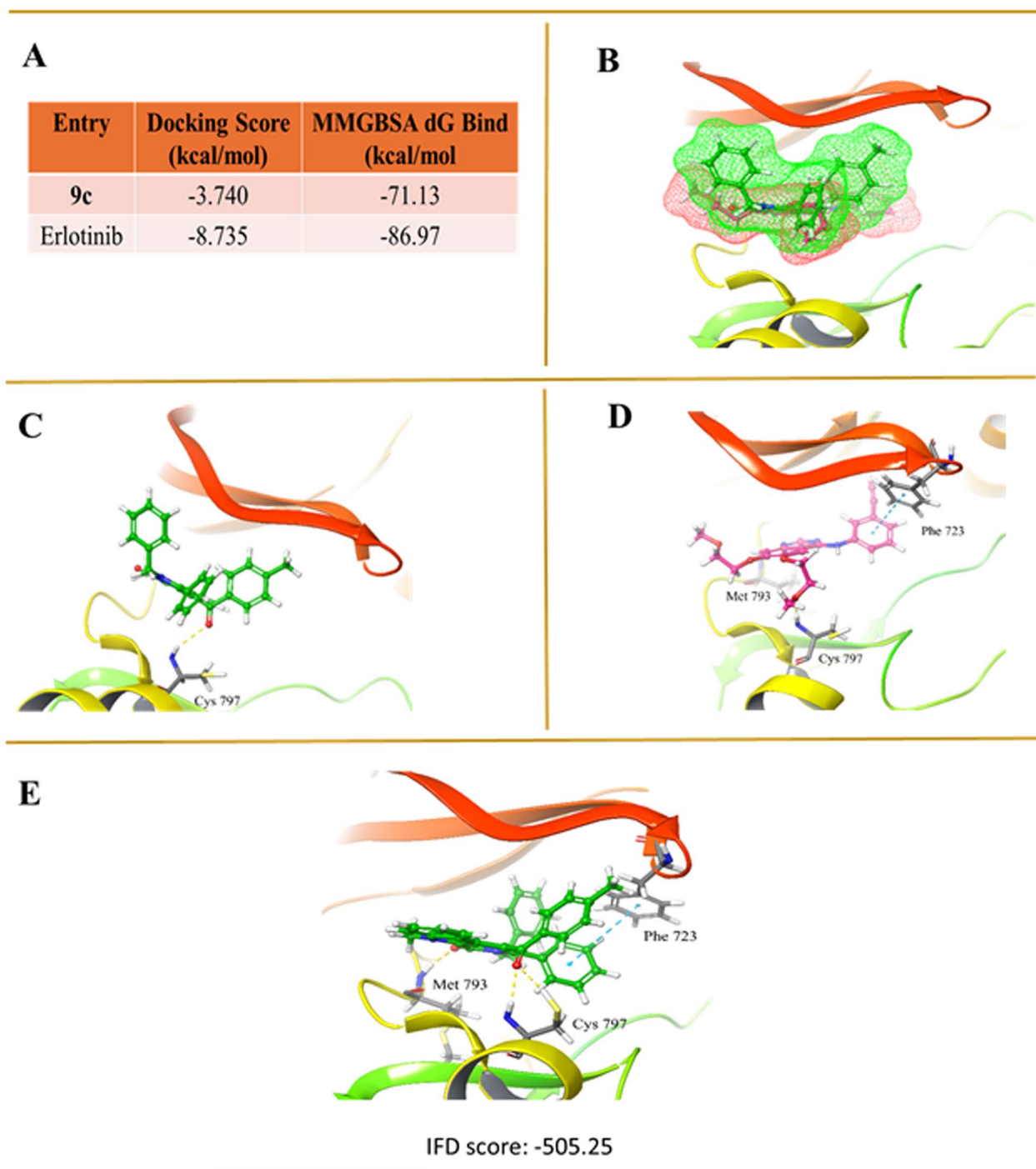


Fig. 8 Compound **9c** attenuates the sphere-forming ability of MDA-MB-231 cells. MDA-MB-231 single-cell suspensions were prepared in 1.5% methylcellulose with 20% FBS-DMEM, seeded onto 1% agarose-coated plates to promote non-adherent growth, and treated with doxorubicin (dox) or compound **9c** (0.5, 1, and 2  $\mu\text{M}$ ) to allow sphere formation. Imaging was performed using fluorescence microscopy. (A) Representative fluorescence images of MDA-MB-231 spheres after 8 days of treatment with dox or **9c**. Scale bar = 100  $\mu\text{m}$ . (B) Quantification of spheroid numbers per microscopic field.



**2.2.7 Molecular docking studies.** Next, we assessed whether **9c** binds to epidermal growth factor receptor (EGFR) and inhibits cancer progression. Rigid docking analysis revealed that **9c** exhibited a binding affinity for EGFR with a docking score of  $-3.74$  kcal mol $^{-1}$ , which was lower than that of the known EGFR inhibitor, erlotinib, which displayed a score of  $-8.735$  kcal mol $^{-1}$  (Fig. 9A). Despite the difference in scores,

both compounds were observed to occupy the same pocket within the hinge region of EGFR. Detailed interaction analysis indicated that **9c** formed a specific interaction with Cys 797 (subdomain V) at the ATP binding site within the hinge region (Fig. 9B). In contrast, erlotinib engaged through a  $\pi$ - $\pi$  stacking interaction with Phe 723 (g-loop) and hydrogen bond interactions with Cys 797 (subdomain V) and Met 793 (hinge region)



**Fig. 9** Molecular docking, MM-GSBA, and IFD-SP of **9c** with EGFR (PDB: 4ZAU). (A) Dock score and binding energy results for **9c** and erlotinib. (B) The binding pocket occupied by **9c** and erlotinib in the EGFR protein. (C) 3D interaction diagram of **9c** after rigid docking. (D) 3D interaction diagram of erlotinib after rigid docking. (E) Interaction diagram of **9c** obtained after IFD-SP.



Table 3 Molecular docking interactions of **9c** and erlotinib

Entry	Interactions
<b>9c</b>	H-bond: Cys 797 Hydrophobic interactions Charged negative: Asp 800 Charge positive: Lys 716, Lys 728 Polar: Thr 790, Gln 791, Ser 720 Hydrophobic: Val 726, Phe 723, Leu 718, Ala 743, Leu 844, Leu 792, Met 793, Pro 794, Phe 795 Glycine: Gly 719, Gly 796
Erlotinib	H-bond: Cys 797, Met 793 $\pi$ - $\pi$ interaction: Phe 723 Hydrophobic interactions Charged positive: Lys 745, Lys 728 Charge negative: Glu 796, Asp 855, Asp 800 Polar: Thr 790, Thr 854, Gln 791 Hydrophobic: Leu 844, Met 766, Ile 744, Ala 743, Leu 788, Ile 789, Leu 792, Pro 794, Phe 795, Leu 718, Val 726 Glycine: Gly 796

(Fig. 9C). To further refine these findings, induced fit docking using standard precision (IFD-SP) was performed in which we got to know that **9c** could form similar interactions to erlotinib, including hydrogen bonds with Cys 797 and Met 793, as well as a  $\pi$ - $\pi$  stacking interaction with Phe 723, due to a positional shift of the G-loop (Fig. 9D). Furthermore, the binding energies were calculated for the docked complex **9c** ( $-71.13$  kcal mol $^{-1}$ ) and erlotinib ( $-86.97$  kcal mol $^{-1}$ ), suggesting a substantial binding potential of **9c** toward EGFR in similar manner to that of erlotinib (Table 3).

### 3. Conclusions

In conclusion, a novel series of 1*H*-pyrido[3,4-*b*]indol-1-one hybrids was thoughtfully designed and synthesized *via* Ru-complex catalyzed annulation reaction involving the indole amides **5(a-d)**, and ynones **8(a-e)** for the first time, followed by characterization through various physicochemical methods. These compounds were assessed for their anticancer properties using the SRB assay and annexin V-FITC/propidium iodide staining to assess apoptosis. Findings indicated that the newly developed hybrid, **9c**, showed substantial cytotoxic activity and a strong ability to induce apoptosis in breast cancer cells, including the particularly aggressive triple-negative breast cancer (TNBC) cells. Moreover, compound **9c** exhibited  $\sim$ 10-fold preference for MDA-MB-231 breast cancer cells over normal HEK-293 kidney and BEAS-2B lung cells, highlighting its enhanced selectivity and therapeutic potential. Compound **9c** also showed elevated apoptosis and exhibited remarkable inhibition of three-dimensional multicellular tumor spheroids formation, indicating its potential to hinder spheroid development. Molecular docking studies indicated that compound **9c** possesses a moderate binding affinity for EGFR, suggesting its potential for targeted therapeutic applications. Taken together, these findings underscore the promise of compound **9c** as

a compelling lead for future innovations in cancer therapeutics. To strengthen its translational relevance, subsequent future studies will focus on comprehensive ADME (Absorption, Distribution, Metabolism, and Excretion) profiling and *in vivo* validation to assess pharmacokinetics, bioavailability, and therapeutic efficacy in relevant animal models.

## 4. Experimental section

### 4.1 Chemistry

Chemicals, reagents, and solvents were sourced from established suppliers such as Spectrochem, Loba Chemie Pvt Ltd, Sigma-Aldrich, and TCI and were utilized without undergoing additional purification processes. Thin-layer chromatography (TLC) was employed to track reaction progress, utilizing pre-coated silica gel 60 F254 glass plates with a medium pore diameter of 60 Å. Visualization and analysis of TLC plates were performed using UV light exposure and anisaldehyde charring solution. Silica gel with a mesh size of 60–120 was utilized for performing column chromatography. An electrothermal melting point apparatus was used to determine the melting points of the compounds. Nuclear magnetic resonance (NMR) spectroscopy data for  $^1\text{H}$  NMR were recorded at 300 MHz, 400 MHz, and 500 MHz frequencies and analyzed with MestReNova software. Chemical shifts are presented in parts per million (ppm), referenced from tetramethyl silane (TMS) at 0 ppm, with solvent resonances identified at 7.26 ppm for CDCl $_3$  and 2.49 ppm for DMSO- $d_6$ .  $^{13}\text{C}$  NMR were recorded at 75 MHz, 101 MHz and 126 MHz and the chemical shifts are also given in ppm, with solvent resonances at 77 ppm for CDCl $_3$  and 39.3 ppm for DMSO- $d_6$ .  $^{19}\text{F}$  NMR was recorded at 376 MHz and 377 MHz with chemical shifts shown in ppm. Spin multiplicities were categorized as singlet (s), doublet (d), triplet (t), quartet (q), or multiplet (m). Coupling constants are expressed in Hertz (Hz). High-resolution mass spectrometry (HRMS) data were acquired using a Varian ESI-QTOF instrument.

**4.1.1 General synthetic procedure for 1-methyl-1*H*-indole-2-carboxamide derivatives [5(a-d)].** The synthesis of 1-methyl-1*H*-indole-2-carboxamide derivatives [5(a-d)] were carried out by following a literature-reported method.<sup>33</sup> The general synthetic route is outlined in Scheme 1A. Under an inert atmosphere, 1-methyl-1*H*-indole-2-carboxylic acid was solubilized in dichloromethane (DCM) at 0 °C. To this solution, 1.2 equivalents of EDC·HCl and 1.5 equivalents of HOBT were added, followed by stirring at 0 °C for 5–10 minutes. Subsequently, 1.5 equivalents of the respective amine introduced into the reaction mixture. The reaction was allowed to proceed at room temperature for 2 hours. Afterward, the crude product was washed with water, and the organic phase was dried over anhydrous Na $_2$ SO $_4$ , followed by the removal of the solvent under vacuum. The crude product was subjected to column chromatographic purification on silica gel (60–120 mesh) using a mixture of 8% ethyl acetate and hexane as the eluent, resulting the compounds **5(a-d)** with good yields.

**4.1.2 General synthetic procedure for 1,3-diphenylprop-2-yn-1-one derivatives [8(a-e)].** The 1,3-diphenylprop-2-yn-1-one derivatives **8(a-e)** were synthesized by following a literature-



reported method with minor modification.<sup>34</sup> The general synthetic route to obtain the ynones is outlined in scheme 1B. CuI (2 mol%) and TMEDA (5 mol%) were added to a two-necked round-bottom flask maintained at 0 °C under nitrogen atmosphere. Benzoyl chloride (1.0 eq.), phenyl acetylene (1.5 eq.), and TEA (3.0 eq.) were introduced to the reaction mixture, and it was stirred at room temperature for 4 hours. After the reaction was complete, the crude product was washed with saturated NH<sub>4</sub>Cl solution. The aqueous layer was extracted with DCM, and the combined organic phases were washed with brine, dried over anhydrous Na<sub>2</sub>SO<sub>4</sub>, and concentrated under vacuum. The resulting crude mixture was purified *via* column chromatography on silica gel (60–120 mesh), with 1% ethyl acetate and hexane as the eluent, yielding compounds **8(a–e)** in good yields.

**4.1.3 General procedure for the synthesis of 1H-pyrido[3,4-b]indol-1-one derivatives [9(a–e), 10(a–e), 11(a–e) and 12(a–e)].** The final 1H-pyrido[3,4-b]indol-1-one hybrids [9(a–e), 10(a–e), 11(a–e) and 12(a–e)] were synthesized *via* a convenient route. The reaction conditions were optimized by screening solvents, catalysts and the additives (Tables S1 and S2). The general and optimized synthetic route to the pyrido-indole-one hybrids is outlined in Scheme 2. To a solution of indole carboxamide [5(a–d)] (1 eq.) in anhydrous THF, Cu(OAc)<sub>2</sub> (2 eq.) was added and stirred for 5 minutes at room temperature. To this the respective ynone **8(a–e)** (1.2 eq.) was added gradually followed by the addition of silver hexafluoroantimonate (3 mol%) and dichloro(*p*-cymene)ruthenium(II) dimer (10 mol%). The reaction mixture was stirred at 75 °C for 24 hours. Upon completion, the solvent was removed under reduced pressure. The crude product was extracted with ethyl acetate and washed with water several times. The organic layers were dried over anhydrous Na<sub>2</sub>SO<sub>4</sub>, followed by concentration under vacuum. The resulting residue was purified by column chromatography on silica gel (60–120 mesh) using 6% ethyl acetate and hexane as the eluent, yielding the pure compounds **9(a–e)**, **10(a–e)**, **11(a–e)** and **12(a–e)**.

**4.1.3.1 4-Benzoyl-2-benzyl-9-methyl-3-phenyl-2,9-dihydro-1H-pyrido[3,4-b]indol-1-one (9a).** Light yellow solid; yield: 62%; melting point: 159–161 °C; <sup>1</sup>H NMR (400 MHz, DMSO-d<sub>6</sub>) δ 7.72 (d, *J* = 8.0 Hz, 3H), 7.54–7.45 (m, 2H), 7.35 (t, *J* = 7.7 Hz, 2H), 7.25–7.17 (m, 5H), 7.12 (t, *J* = 7.5 Hz, 2H), 7.07–7.02 (m, 3H), 6.87 (d, *J* = 6.9 Hz, 2H), 5.20 (s, 2H), 4.36 (s, 3H). <sup>13</sup>C NMR (101 MHz, DMSO-d<sub>6</sub>) δ 195.5, 156.1, 141.3, 138.0, 137.7, 137.5, 134.2, 132.9, 130.9, 129.7, 129.4, 129.2, 128.7, 128.2, 127.3, 127.2, 126.5, 125.9, 121.9, 120.9, 120.5, 119.9, 115.7, 111.5, 48.0, 31.8. HRMS (ESI) calcd for C<sub>32</sub>H<sub>24</sub>O<sub>2</sub>N<sub>2</sub> [M + H]<sup>+</sup>: 469.1916; found: 469.1911.

**4.1.3.2 2-Benzyl-4-(4-methoxybenzoyl)-9-methyl-3-phenyl-2,9-dihydro-1H-pyrido[3,4-b]indol-1-one (9b).** White solid; yield: 64%; melting point: 165–167 °C; <sup>1</sup>H NMR (400 MHz, DMSO-d<sub>6</sub>) δ 7.71 (d, *J* = 8.8 Hz, 2H), 7.68 (s, 1H), 7.46 (t, *J* = 7.2 Hz, 1H), 7.23–7.16 (m, 5H), 7.13 (t, *J* = 7.5 Hz, 2H), 7.09–7.01 (m, 3H), 6.88–6.84 (m, 4H), 5.17 (s, 2H), 4.33 (s, 3H), 3.74 (s, 3H). <sup>13</sup>C NMR (126 MHz, DMSO-d<sub>6</sub>) δ 193.6, 164.0, 156.1, 141.3, 138.0, 137.1, 133.0, 132.3, 130.8, 130.3, 129.4, 128.7, 128.2, 127.3, 126.5, 125.9, 121.9, 120.9, 120.6, 119.9, 115.9, 114.5, 111.5, 56.0, 48.0, 31.8. HRMS (ESI) calcd for C<sub>33</sub>H<sub>26</sub>O<sub>3</sub>N<sub>2</sub> [M + H]<sup>+</sup>: 499.2022; found: 499.2020.

**4.1.3.3 2-Benzyl-9-methyl-4-(4-methylbenzoyl)-3-phenyl-2,9-dihydro-1H-pyrido[3,4-b]indol-1-one (9c).** Yellow solid; yield: 68%; melting point: 185–187 °C; <sup>1</sup>H NMR (400 MHz, DMSO-d<sub>6</sub>) δ 7.72 (d, *J* = 8.5 Hz, 1H), 7.64 (d, *J* = 8.1 Hz, 2H), 7.47 (t, *J* = 7.7 Hz, 1H), 7.24–7.16 (m, 7H), 7.13–7.01 (m, 5H), 6.87 (d, *J* = 6.9 Hz, 2H), 5.19 (s, 2H), 4.36 (s, 3H), 2.28 (s, 3H). <sup>13</sup>C NMR (126 MHz, DMSO-d<sub>6</sub>) δ 194.9, 156.1, 144.8, 141.3, 138.0, 137.3, 135.0, 133.0, 130.9, 129.9, 129.8, 129.4, 128.7, 128.1, 127.2, 126.5, 125.9, 121.9, 120.9, 120.6, 119.9, 115.8, 111.5, 48.0, 31.8, 21.6. HRMS (ESI) calcd for C<sub>33</sub>H<sub>26</sub>O<sub>2</sub>N<sub>2</sub> [M + H]<sup>+</sup>: 483.2073; found: 483.2068.

**4.1.3.4 2-Benzyl-9-methyl-3-phenyl-4-(4-(trifluoromethyl)benzoyl)-2,9-dihydro-1H-pyrido[3,4-b]indol-1-one (9d).** Light orange solid; yield: 60%; melting point: 206–209 °C; <sup>1</sup>H NMR (300 MHz, DMSO-d<sub>6</sub>) δ 7.84 (d, *J* = 8.1 Hz, 2H), 7.73 (d, *J* = 8.5 Hz, 1H), 7.67 (d, *J* = 8.2 Hz, 2H), 7.49 (t, *J* = 7.2 Hz, 1H), 7.26–7.18 (m, 5H), 7.12–7.01 (m, 5H), 6.87 (d, *J* = 6.0 Hz, 2H), 5.19 (s, 2H), 4.35 (s, 3H). <sup>13</sup>C NMR (126 MHz, DMSO-d<sub>6</sub>) δ 195.1, 159.4, 156.2, 141.3, 140.9, 138.7, 137.8, 132.7, 131.0, 130.2, 129.6, 128.7, 128.2, 127.4, 127.3, 126.5, 126.1, 126.0, 121.9, 121.1, 120.3, 119.8, 115.1, 111.6, 48.1, 31.8. <sup>19</sup>F NMR (377 MHz, DMSO-d<sub>6</sub>) δ –61.7. HRMS (ESI) calcd for C<sub>33</sub>H<sub>23</sub>O<sub>2</sub>N<sub>2</sub>F<sub>3</sub> [M + H]<sup>+</sup>: 537.1790; found: 537.1784.

**4.1.3.5 2-Benzyl-4-(4-fluorobenzoyl)-9-methyl-3-phenyl-2,9-dihydro-1H-pyrido[3,4-b]indol-1-one (9e).** Yellow solid; yield: 59%; melting point: 173–175 °C; <sup>1</sup>H NMR (400 MHz, DMSO-d<sub>6</sub>) δ 7.86 (q, *J* = 12 Hz, 2H), 7.79 (d, *J* = 8.4 Hz, 1H), 7.55 (t, *J* = 7.6 Hz, 1H), 7.34–7.23 (m, 6H), 7.23–7.11 (m, 6H), 6.94 (d, *J* = 6.9 Hz, 2H), 5.26 (s, 2H), 4.42 (s, 3H). <sup>13</sup>C NMR (126 MHz, DMSO-d<sub>6</sub>) δ 194.1, 166.6, 164.6, 156.1, 141.3, 137.9, 134.3, 132.9, 132.8, 132.7, 130.9, 129.5, 128.7, 128.2, 127.3, 126.5, 126.0, 121.9, 121.0, 120.4, 119.9, 116.3, 116.2, 115.4, 111.6, 48.1, 31.8. <sup>19</sup>F NMR (377 MHz, DMSO-d<sub>6</sub>) δ –104.6. HRMS (ESI) calcd for C<sub>32</sub>H<sub>23</sub>O<sub>2</sub>N<sub>2</sub>F [M + H]<sup>+</sup>: 487.1822; found: 487.1817.

**4.1.3.6 4-Benzoyl-9-methyl-2-phenethyl-3-phenyl-2,9-dihydro-1H-pyrido[3,4-b]indol-1-one (10a).** Light yellow solid; yield: 63%; melting point: 235–237 °C; <sup>1</sup>H NMR (400 MHz, DMSO-d<sub>6</sub>) δ 7.62 (d, *J* = 7.7 Hz, 2H), 7.57 (d, *J* = 7.8 Hz, 1H), 7.44 (t, *J* = 7.3 Hz, 1H), 7.38 (t, *J* = 7.7 Hz, 1H), 7.33–7.27 (m, 3H), 7.18 (t, *J* = 7.3 Hz, 2H), 7.15–7.04 (m, 6H), 6.92 (t, *J* = 7.6 Hz, 1H), 6.74 (d, *J* = 7.1 Hz, 2H), 4.34 (s, 3H), 4.02 (t, *J* = 6.8 Hz, 2H), 2.87 (t, *J* = 7.6 Hz, 2H). <sup>13</sup>C NMR (101 MHz, DMSO-d<sub>6</sub>) δ 200.2, 160.7, 145.9, 143.1, 142.6, 142.1, 138.4, 137.7, 135.5, 134.2, 134.0, 133.5, 133.4, 132.9, 131.7, 131.3, 130.7, 126.9, 125.3, 125.2, 124.8, 120.4, 115.5, 51.9, 39.5, 36.3. HRMS (ESI) calcd for C<sub>33</sub>H<sub>26</sub>O<sub>2</sub>N<sub>2</sub> [M + H]<sup>+</sup>: 483.2073; found: 483.2068.

**4.1.3.7 4-(4-Methoxybenzoyl)-9-methyl-2-phenethyl-3-phenyl-2,9-dihydro-1H-pyrido[3,4-b]indol-1-one (10b).** White solid; yield: 64%; melting point: 174–176 °C; <sup>1</sup>H NMR (500 MHz, DMSO-d<sub>6</sub>) δ 7.73 (d, *J* = 8.7 Hz, 2H), 7.70 (s, 1H), 7.46 (t, *J* = 7.7 Hz, 1H), 7.38–7.28 (m, 3H), 7.21–7.14 (m, 6H), 7.02 (t, *J* = 7.5 Hz, 1H), 6.90 (d, *J* = 8.9 Hz, 2H), 6.80 (d, *J* = 6.8 Hz, 2H), 4.39 (s, 3H), 4.01 (t, *J* = 5 Hz, 2H), 3.78 (s, 3H), 2.87 (t, *J* = 10 Hz, 2H). <sup>13</sup>C NMR (101 MHz, DMSO-d<sub>6</sub>) δ 193.6, 164.0, 155.8, 141.2, 138.7, 137.0, 133.2, 132.3, 131.0, 130.5, 129.4, 128.9, 128.8, 128.4, 127.1, 126.9, 125.9, 121.9, 120.8, 120.5, 119.9, 115.6, 114.5, 111.4, 56.0,



47.1, 34.5, 31.7. HRMS (ESI) calcd for  $C_{34}H_{28}O_3N_2$   $[M + H]^+$ : 513.2178; found: 513.2180.

**4.1.3.8 9-Methyl-4-(4-methylbenzoyl)-2-phenethyl-3-phenyl-2,9-dihydro-1H-pyrido[3,4-b]indol-1-one (10c).** Yellow solid; yield: 62%; melting point: 220–221 °C;  $^1H$  NMR (400 MHz, DMSO- $d_6$ )  $\delta$  7.80 (d,  $J = 8.5$  Hz, 1H), 7.73 (d,  $J = 8.1$  Hz, 2H), 7.55 (t,  $J = 7.7$  Hz, 1H), 7.43–7.36 (m, 3H), 7.33–7.25 (m, 7H), 7.22 (d,  $J = 8.1$  Hz, 1H), 7.10 (t,  $J = 7.5$  Hz, 1H), 6.89 (d,  $J = 6.6$  Hz, 2H), 4.48 (s, 3H), 4.15 (t,  $J = 8$  Hz, 2H), 2.96 (t,  $J = 8$  Hz, 2H), 2.39 (s, 3H).  $^{13}C$  NMR (126 MHz, DMSO- $d_6$ )  $\delta$  201.3, 194.8, 155.8, 144.8, 141.2, 138.7, 137.2, 135.1, 133.1, 131.0, 130.0, 129.8, 129.5, 128.9, 128.8, 128.4, 127.1, 126.9, 125.9, 121.9, 120.8, 120.4, 119.9, 115.5, 111.5, 47.1, 34.5, 31.8, 21.7. HRMS (ESI) calcd for  $C_{34}H_{28}O_2N_2$   $[M + H]^+$ : 497.2229; found: 497.2229.

**4.1.3.9 9-Methyl-2-phenethyl-3-phenyl-4-(4-(trifluoromethyl)benzoyl)-2,9-dihydro-1H-pyrido[3,4-b]indol-1-one (10d).** Yellow solid; yield: 60%; melting point: 211–213 °C;  $^1H$  NMR (400 MHz, DMSO- $d_6$ )  $\delta$  7.85 (d,  $J = 8.0$  Hz, 2H), 7.75 (d,  $J = 8.5$  Hz, 1H), 7.71 (d,  $J = 8.3$  Hz, 2H), 7.49 (t,  $J = 7.7$  Hz, 1H), 7.33 (t,  $J = 7.3$  Hz, 1H), 7.26 (t,  $J = 7.4$  Hz, 2H), 7.23–7.13 (m, 6H), 7.06 (t,  $J = 7.5$  Hz, 1H), 6.80 (d,  $J = 6.7$  Hz, 2H), 4.40 (s, 3H), 4.03 (t,  $J = 8$  Hz, 2H), 2.87 (t,  $J = 8$  Hz, 2H).  $^{13}C$  NMR (101 MHz, DMSO- $d_6$ )  $\delta$  195.0, 155.8, 141.3, 141.0, 138.6, 138.5, 132.9, 131.1, 130.3, 129.7, 129.0, 128.8, 128.4, 127.3, 126.9, 126.1, 126.0, 121.9, 121.0, 120.2, 119.7, 114.8, 111.6, 47.2, 34.5, 31.8.  $^{19}F$  NMR (377 MHz, DMSO- $d_6$ )  $\delta$  -61.6. HRMS (ESI) calcd for  $C_{34}H_{25}O_2N_2F_3$   $[M + H]^+$ : 551.1946; found: 551.1949.

**4.1.3.10 4-(4-Fluorobenzoyl)-9-methyl-2-phenethyl-3-phenyl-2,9-dihydro-1H-pyrido[3,4-b]indol-1-one (10e).** Yellow solid; yield: 58%; melting point: 183–185 °C;  $^1H$  NMR (300 MHz, DMSO- $d_6$ )  $\delta$  7.78 (q,  $J = 18$  Hz, 2H), 7.70 (d,  $J = 8.4$  Hz, 1H), 7.46 (t,  $J = 7.4$  Hz, 1H), 7.37–7.24 (m, 3H), 7.18–7.14 (m, 8H), 7.03 (t,  $J = 9$  Hz, 1H), 6.78 (d,  $J = 6.1$  Hz, 2H), 4.37 (s, 3H), 4.01 (t,  $J = 6$  Hz, 2H), 2.85 (t,  $J = 9$  Hz, 2H).  $^{13}C$  NMR (126 MHz, DMSO- $d_6$ )  $\delta$  194.0, 166.6, 164.6, 141.2, 138.6, 137.7, 134.4, 133.0, 132.9, 132.8, 131.0, 129.6, 128.9, 128.8, 128.4, 127.2, 126.9, 125.9, 121.8, 120.9, 120.3, 119.8, 116.4, 116.2, 115.1, 111.5, 47.1, 34.5, 31.8.  $^{19}F$  NMR (377 MHz, DMSO- $d_6$ )  $\delta$  -104.6. HRMS (ESI) calcd for  $C_{33}H_{25}O_2N_2F$   $[M + H]^+$ : 501.1978; found: 501.1973.

**4.1.3.11 4-Benzoyl-2-butyl-9-methyl-3-phenyl-2,9-dihydro-1H-pyrido[3,4-b]indol-1-one (11a).** Pale yellow solid; yield: 50%; melting point: 173–180 °C;  $^1H$  NMR (500 MHz,  $CDCl_3$ )  $\delta$  7.67 (d,  $J = 7.5$  Hz, 2H), 7.49–7.37 (m, 4H), 7.29–7.23 (m, 5H), 7.21 (s, 2H), 7.01 (t,  $J = 7.3$  Hz, 1H), 4.43 (s, 3H), 3.99 (t,  $J = 5$  Hz, 2H), 1.64–1.56 (m, 2H), 1.18–1.11 (m, 2H), 0.73 (t,  $J = 7.3$  Hz, 3H);  $^{13}C$  NMR (75 MHz,  $CDCl_3$ )  $\delta$  196.2, 156.4, 141.3, 138.2, 137.4, 133.1, 130.7, 129.3, 128.9, 128.3, 128.0, 126.7, 126.2, 122.6, 120.9, 120.3, 120.2, 116.2, 110.0, 45.4, 31.4, 31.1, 20.0, 13.4; HRMS (ESI) calcd for  $C_{29}H_{26}N_2O_2$   $[M + H]^+$ : 435.2072; found: 435.2049.

**4.1.3.12 2-Butyl-4-(4-methoxybenzoyl)-9-methyl-3-phenyl-2,9-dihydro-1H-pyrido[3,4-b]indol-1-one (11b).** Pale yellow solid; yield: 52%; melting point: 134–139 °C;  $^1H$  NMR (400 MHz,  $CDCl_3$ )  $\delta$  7.70 (d,  $J = 8.3$  Hz, 2H), 7.50–7.25 (m, 8H), 7.00 (t,  $J = 7.0$  Hz, 1H), 6.75 (d,  $J = 8.4$  Hz, 2H), 4.42 (s, 3H), 3.93 (d,  $J = 9.1$  Hz, 2H), 3.79 (s, 3H), 1.65–1.55 (m, 2H), 1.18–1.102 (m, 2H), 0.73 (t,  $J = 7.2$  Hz, 3H);  $^{13}C$  NMR (75 MHz,  $CDCl_3$ )  $\delta$  194.4, 163.7, 156.4, 141.3, 136.9, 133.2, 131.9, 131.0, 130.6, 128.9, 128.0,

126.7, 126.2, 122.7, 122.2, 121.0, 120.3, 116.3, 114.9, 113.6, 109.9, 55.4, 45.4, 31.4, 31.1, 20.0, 13.4; HRMS (ESI) calcd for  $C_{30}H_{28}N_2O_3$   $[M + H]^+$ : 465.2178; found: 465.2163.

**4.1.3.13 2-Butyl-9-methyl-4-(4-methylbenzoyl)-3-phenyl-2,9-dihydro-1H-pyrido[3,4-b]indol-1-one (11c).** Pale yellow solid; yield: 55%; melting point: 149–152 °C;  $^1H$  NMR (300 MHz,  $CDCl_3$ )  $\delta$  7.60 (d,  $J = 8.2$  Hz, 2H), 7.45 (t,  $J = 8.2$  Hz, 2H), 7.36 (d,  $J = 8.2$  Hz, 1H), 7.23 (m, 5H), 7.06 (d,  $J = 8.0$  Hz, 2H), 7.00 (t,  $J = 6.4$  Hz, 1H), 4.42 (s, 3H), 3.94 (t,  $J = 6$  Hz, 2H), 2.32 (s, 3H), 1.56 (d,  $J = 7.9$  Hz, 2H), 1.21–1.08 (m, 2H), 0.73 (t,  $J = 7.4$  Hz, 3H);  $^{13}C$  NMR (75 MHz,  $CDCl_3$ )  $\delta$  195.7, 156.4, 144.2, 141.3, 137.1, 135.5, 133.2, 130.7, 129.6, 129.1, 128.9, 128.0, 126.7, 126.2, 122.7, 120.9, 120.3, 116.3, 109.9, 45.4, 31.4, 31.1, 21.7, 20.0, 13.4; HRMS (ESI) calcd for  $C_{30}H_{28}N_2O_2$   $[M + H]^+$ : 449.2229; found: 449.2217.

**4.1.3.14 2-Butyl-9-methyl-3-phenyl-4-(4-(trifluoromethyl)benzoyl)-2,9-dihydro-1H-pyrido[3,4-b]indol-1-one (11d).** Yellow solid; yield: 69%; melting point: 169–175 °C;  $^1H$  NMR (400 MHz,  $CDCl_3$ )  $\delta$  7.70 (d,  $J = 8.2$  Hz, 2H), 7.50–7.45 (m, 4H), 7.41 (d,  $J = 8.0$  Hz, 1H), 7.23–7.15 (m, 5H), 7.05 (t,  $J = 7.3$  Hz, 1H), 4.43 (s, 3H), 3.95 (t,  $J = 4$  Hz, 2H), 1.66–1.58 (m, 2H), 1.19–1.10 (m, 2H), 0.73 (t,  $J = 7.3$  Hz, 3H);  $^{13}C$  NMR (126 MHz,  $CDCl_3$ )  $\delta$  195.4, 156.4, 141.3, 141.2, 138.1, 133.9, 132.9, 130.7, 129.3, 129.2, 128.1, 126.9, 126.3, 125.3, 125.2, 122.4, 120.6, 120.5, 120.0, 115.6, 110.1, 45.4, 31.5, 31.0, 20.0, 13.4;  $^{19}F$  NMR (377 MHz,  $CDCl_3$ )  $\delta$  -63.1; HRMS (ESI) calcd for  $C_{30}H_{25}F_3N_2O_2$   $[M + H]^+$ : 503.1946; found: 503.1940.

**4.1.3.15 2-Butyl-4-(4-fluorobenzoyl)-9-methyl-3-phenyl-2,9-dihydro-1H-pyrido[3,4-b]indol-1-one (11e).** Pale yellow solid; yield: 65%; melting point: 148–152 °C;  $^1H$  NMR (400 MHz,  $CDCl_3$ )  $\delta$  7.70 (q,  $J = 8.6, 5.5$  Hz, 2H), 7.46 (q,  $J = 8.5$  Hz, 2H), 7.38 (d,  $J = 8.1$  Hz, 1H), 7.24 (m, 5H), 7.03 (t,  $J = 6.6$  Hz, 1H), 6.92 (t,  $J = 8.6$  Hz, 2H), 4.43 (s, 3H), 3.98 (t, 8 Hz, 2H), 1.60–1.53 (m, 2H), 1.19–1.10 (m, 2H), 0.73 (t,  $J = 7.4$  Hz, 3H);  $^{13}C$  NMR (75 MHz,  $CDCl_3$ )  $\delta$  194.6, 167.4, 164.0, 156.4, 141.3, 137.4, 134.6, 133.1, 132.1, 131.9, 130.6, 129.0, 128.1, 126.8, 122.5, 120.4, 120.1, 115.6, 115.4, 110.1, 45.4, 31.5, 31.0, 20.0, 13.4;  $^{19}F$  NMR (377 MHz,  $CDCl_3$ )  $\delta$  -104.4; HRMS (ESI) calcd for  $C_{29}H_{25}FN_2O_2$   $[M + H]^+$ : 453.1978; found: 453.1973.

**4.1.3.16 2-(Benzo[d]thiazol-2-yl)-4-benzoyl-9-methyl-3-phenyl-2,9-dihydro-1H-pyrido[3,4-b]indol-1-one (12a).** Pale yellow solid; yield: 52%; melting point: 302–309 °C;  $^1H$  NMR (500 MHz,  $CDCl_3$ )  $\delta$  7.79 (d,  $J = 7.3$  Hz, 1H), 7.61 (d,  $J = 7.5$  Hz, 2H), 7.55–7.45 (m, 3H), 7.35–7.27 (m, 8H), 7.16 (t,  $J = 7.8$  Hz, 2H), 6.98 (t,  $J = 8.0$  Hz, 1H), 6.64 (d,  $J = 8.2$  Hz, 1H), 4.46 (s, 3H);  $^{13}C$  NMR (126 MHz,  $CDCl_3$ )  $\delta$  195.3, 158.5, 156.6, 149.6, 141.6, 137.5, 136.7, 136.6, 133.5, 131.8, 131.3, 129.5, 128.8, 128.4, 127.5, 127.4, 126.2, 126.0, 125.4, 124.0, 122.8, 121.7, 121.6, 121.0, 120.4, 116.8, 110.3, 31.6; HRMS (ESI) calcd for  $C_{32}H_{21}N_3O_2S$   $[M + H]^+$ : 512.1432; found: 512.1377.

**4.1.3.17 2-(Benzo[d]thiazol-2-yl)-4-(4-methoxybenzoyl)-9-methyl-3-phenyl-2,9-dihydro-1H-pyrido[3,4-b]indol-1-one (12b).** Pale yellow solid; yield: 64%; melting point: 272–276 °C;  $^1H$  NMR (500 MHz, DMSO- $d_6$ )  $\delta$  8.03 (d,  $J = 8.4$  Hz, 1H), 7.88 (q,  $J = 15.4, 8.3$  Hz, 3H), 7.76 (d,  $J = 8.5$  Hz, 1H), 7.53–7.43 (m, 3H), 7.26 (d,  $J = 7.7$  Hz, 3H), 7.10 (t,  $J = 7.6$  Hz, 1H), 6.99 (s, 3H), 6.90 (d,  $J = 8.9$  Hz, 2H), 4.32 (s, 3H), 3.77 (s, 3H);  $^{13}C$  NMR (101 MHz,



DMSO- $d_6$ )  $\delta$  193.0, 164.2, 159.5, 156.2, 149.4, 141.4, 136.7, 136.2, 132.5, 132.2, 131.3, 130.1, 129.1, 127.8, 127.7, 126.8, 126.5, 125.2, 123.6, 122.8, 122.0, 121.4, 121.2, 120.0, 116.5, 114.6, 111.8, 56.0, 31.9; HRMS (ESI) calcd for  $C_{33}H_{23}N_3O_3S$   $[M + H]^+$ : 542.1538; found: 542.1481.

**4.1.3.18** 2-(Benzo[d]thiazol-2-yl)-9-methyl-4-(4-methylbenzoyl)-3-phenyl-2,9-dihydro-1H-pyrido[3,4-b]indol-1-one (**12c**). Pale yellow solid; yield: 63%; melting point: 289–295 °C;  $^1H$  NMR (500 MHz, DMSO- $d_6$ )  $\delta$  8.03 (d,  $J$  = 7.6 Hz, 1H), 7.89 (d,  $J$  = 7.1 Hz, 1H), 7.78 (t,  $J$  = 8.1 Hz, 3H), 7.54–7.42 (m, 3H), 7.28–7.18 (m, 5H), 7.09 (t,  $J$  = 7.6 Hz, 1H), 6.99 (s, 3H), 4.32 (s, 3H), 2.29 (s, 3H);  $^{13}C$  NMR (101 MHz,  $CDCl_3$ )  $\delta$  194.8, 158.6, 156.6, 149.7, 144.6, 141.5, 136.6, 136.4, 134.9, 131.9, 131.2, 129.8, 129.2, 128.8, 127.5, 127.3, 126.2, 125.9, 125.4, 124.0, 122.9, 121.7, 121.5, 121.0, 120.4, 116.9, 110.3, 31.5, 21.7; HRMS (ESI) calcd for  $C_{33}H_{23}N_3O_2S$   $[M + H]^+$ : 526.1589; found: 526.1531.

**4.1.3.19** 2-(Benzo[d]thiazol-2-yl)-9-methyl-3-phenyl-4-(4-(trifluoromethyl)benzoyl)-2,9-dihydro-1H-pyrido[3,4-b]indol-1-one (**12d**). Yellow solid; yield: 66%; melting point: 264–270 °C;  $^1H$  NMR (400 MHz, DMSO- $d_6$ )  $\delta$  8.03 (t,  $J$  = 8.8 Hz, 3H), 7.90 (d,  $J$  = 7.5 Hz, 1H), 7.80 (d,  $J$  = 8.6 Hz, 1H), 7.72 (d,  $J$  = 8.3 Hz, 2H), 7.55 (t,  $J$  = 7.2 Hz, 1H), 7.51–7.42 (m, 2H), 7.31 (d,  $J$  = 8.2 Hz, 1H), 7.24 (m, 2H), 7.14 (t,  $J$  = 7.2 Hz, 1H), 6.97 (t,  $J$  = 4 Hz, 3H), 4.34 (s, 3H);  $^{13}C$  NMR (101 MHz,  $CDCl_3$ )  $\delta$  194.5, 158.2, 156.5, 149.6, 142.3, 141.6, 140.5, 137.4, 136.5, 131.6, 131.3, 129.5, 129.1, 127.7, 127.6, 126.3, 126.1, 125.5, 125.4, 124.0, 122.6, 121.6, 121.3, 121.2, 120.3, 116.2, 110.5, 31.6;  $^{19}F$  NMR (376 MHz, DMSO- $d_6$ )  $\delta$  -61.7; HRMS (ESI) calcd for  $C_{33}H_{20}F_3N_3O_2S$   $[M + H]^+$ : 580.1306; found: 580.1254.

**4.1.3.20** 2-(Benzo[d]thiazol-2-yl)-4-(4-fluorobenzoyl)-9-methyl-3-phenyl-2,9-dihydro-1H-pyrido[3,4-b]indol-1-one (**12e**). Pale yellow solid; yield: 61%; melting point: 320–325 °C;  $^1H$  NMR (400 MHz, DMSO- $d_6$ )  $\delta$  8.04 (d,  $J$  = 7.4 Hz, 1H), 7.95 (q,  $J$  = 8 Hz, 2H), 7.89 (d,  $J$  = 8.3 Hz, 1H), 7.78 (d,  $J$  = 8.5 Hz, 1H), 7.55–7.42 (m, 3H), 7.30–7.23 (m, 3H), 7.19 (t,  $J$  = 8.7 Hz, 2H), 7.12 (t,  $J$  = 7.5 Hz, 1H), 7.02–6.97 (m, 3H), 4.33 (s, 3H);  $^{13}C$  NMR (101 MHz, DMSO- $d_6$ )  $\delta$  193.3, 158.7, 156.2, 149.4, 141.5, 136.7, 136.4, 132.5, 132.4, 132.2, 131.8, 131.1, 129.0, 127.6, 126.5, 126.3, 125.2, 123.6, 122.3, 122.1, 121.2, 121.1, 120.0, 116.2, 116.0, 115.8, 111.0, 31.7;  $^{19}F$  NMR (377 MHz, DMSO- $d_6$ )  $\delta$  -104.2; HRMS (ESI) calcd for  $C_{32}H_{20}FN_3O_2S$   $[M + H]^+$ : 530.1338; found: 530.1292.

## 4.2 Biology

**4.2.1 In vitro anticancer studies (cell culture conditions).** MCF-7 cells (human breast adenocarcinoma, estrogen and progesterone receptor-positive, luminal A subtype), 4T1 cells (murine triple-negative breast cancer), MDA-MB-231 cells (human triple-negative breast cancer), HEK-293 cells (human embryonic kidney) and BEAS-2B (normal lung epithelial cell) were sourced from the American Type Culture Collection (ATCC, USA). These cells were cultured in Dulbecco's Modified Eagle Medium (DMEM) supplemented with 10% fetal bovine serum (FBS) and 1% penicillin–streptomycin. Subculturing was carried out using  $1 \times$  trypsin–EDTA. Cells were maintained at 37 °C in a humidified incubator with 5%  $CO_2$ .

**4.2.2 Sulforhodamine B (SRB) cytotoxicity assay.** The cytotoxicity of the test compounds was assessed using the SRB colorimetric assay, adhering to a standard protocol with slight modifications. MCF-7, 4T1, MDA-MB-231, HEK-293 and BEAS-2B cells were cultivated in 96-well plates (3000 cells per well) with each well containing 100  $\mu$ L of complete media. After a 24-hour attachment period, cells were treated with the test compounds at a final concentration of 25  $\mu$ M for 48 hours. Post incubation, cells were fixed using 100  $\mu$ L of chilled 10% trichloroacetic acid (TCA) per well and stored at 4 °C for 1 hour. Wells were then washed thoroughly with tap water and left to air dry. Fixed cells were stained with 0.057% (w/v) SRB solution for 30 minutes in the dark at room temperature. Unbound dye was removed by rinsing with 1% acetic acid, and plates were left to dry completely. Bound dye was solubilized using 200  $\mu$ L of Tris base solution (pH 10.5), and absorbance was recorded at 510 nm using a microplate reader (Biotek, USA). For dose-response studies, cells were treated with varying concentrations of the test compounds (0.39–25  $\mu$ M), and  $IC_{50}$  values were calculated using GraphPad Prism 9.0 *via* non-linear regression analysis.

**4.2.3 Cell cycle analysis.** MCF-7 and 4T1 cells were seeded in 12-well plates at a density of  $1 \times 10^5$  cells per well and incubated for 24 hours to allow attachment. Following attachment, the cells were treated with test compound **9c** at 0.25, 0.5, and 1  $\mu$ M concentrations for an additional 24 hours. After treatment, cells were harvested, washed with PBS, and stained using FxCycle™ PI/RNase staining solution (F10797; Invitrogen, Oregon, USA) for DNA content analysis. The samples were then analyzed by flow cytometry (Becton Dickinson FACS Calibur), and cell cycle distribution in the G1, S, and G2/M phases was determined based on fluorescence intensity using predefined gating methods.

**4.2.4 Annexin V-FITC/PI assay.** To quantify apoptotic cell death, MCF-7 and 4T1 cells were subjected to Annexin V-FITC and propidium iodide (PI) dual staining. The cells were seeded in 12-well plates at a density of  $1 \times 10^5$  cells per well and allowed to adhere for 24 hours. Afterward, the cells were treated with the test compound **9c** at various concentrations for 24 hours. Following treatment, cells were collected, washed with PBS, and resuspended in Annexin V binding buffer containing Annexin V-FITC and PI (BioLegend). The staining was conducted in the dark for 20 minutes at room temperature. The samples were analyzed by flow cytometry (Becton Dickinson FACS Accuri), and the percentages of viable, early apoptotic, late apoptotic, and necrotic cells were determined.

**4.2.5 Gene expression analysis by RT-qPCR.** U87MG cells were treated with varying concentrations of compound **9c** for 48 hours, followed by total RNA extraction using RNA ISO-PLUS reagent, as previously described. The concentration and purity of the isolated RNA were evaluated using a NanoDrop 2000/2000C spectrophotometer (Thermo Scientific). Subsequently, 2  $\mu$ g of total RNA was reverse-transcribed into complementary DNA (cDNA) using a commercially available reverse transcription kit (Takara Bio India), according to the manufacturer's protocol. Quantitative real-time PCR (RT-qPCR) was then



performed to analyze the expression levels of BCL2 and Survivin genes. Gene expression was quantified using the  $2^{-\Delta\Delta C_t}$  method, with Beta-2 microglobulin ( $\beta 2M$ ) serving as the internal reference (housekeeping) gene.

**4.2.6 3D spheroid formation assay.** To assess the sphere-forming ability, a semi-solid culture method using methylcellulose assay was adopted as described earlier.<sup>43</sup> A base layer of 1% agarose (with DMEM media) was prepared in 6-well culture plates and allowed to solidify at room temperature. MDA-MB-231 cells were dissociated into a single-cell suspension and resuspended in 1.5% methylcellulose prepared in DMEM supplemented with 20% FBS. Cells were seeded onto the agarose base at a density of  $1 \times 10^5$  cells per well, and cells were treated with either doxorubicin or compound **9c** (in three doses), then cells were incubated under standard conditions for 8 days to allow spheroid formation. Spheroid morphology and size were assessed using fluorescence microscopy, and quantitative analysis was performed with ImageJ software.

**4.2.7 Molecular docking and MM-GBSA.** Molecular docking was employed to investigate the interaction of **9c** with EGFR (PDB: 4ZAU)<sup>44</sup> to evaluate its potential inhibitory activity. Glide module<sup>45</sup> was utilized to obtain a grid of 20 Å around the AZD9291 (co-crystallized ligand) in Chain A of EGFR, facilitating extra precision docking of **9c**. To further evaluate the binding propensity of the complexes, MM-GBSA calculations<sup>46</sup> were performed using the VSGB solvent model and the OPLS3e force field. Additionally, induced fit docking (IFD) was performed with standard precision to account for receptor-ligand flexibility, generating up to 20 protein-ligand conformations with a van der Waals scaling factor of 0.50.

## Author contributions

B. N. B. and A. S. B. conceptualized and supervised the study. The methodology development, reaction optimization, biological evaluation, experimental data analysis and organization were carried out by M. P. K., T. S., V. D. P., N. S. and H. K. B. performed the molecular docking studies. T. S., with valuable input from B. N. B. and A. S. B., led the study's formal analysis, manuscript drafting. All authors actively engaged in result discussions, contributed to refining the final manuscript, and collectively approved it for publication.

## Conflicts of interest

There are no conflicts to declare.

## Data availability

CCDC 2446994 contains the supplementary crystallographic data for this paper.<sup>47</sup>

All the data generated or analysed during this study are included in this manuscript and its SI. Supplementary information is available. See DOI: <https://doi.org/10.1039/d5ra06548h>.

## Acknowledgements

The authors gratefully acknowledge the CSIR-Indian Institute of Chemical Technology, Hyderabad, India, for providing essential research facilities. Dr B. N. B. and M. P. K. would like to thank the Council of Scientific and Industrial Research (CSIR) for research funding (HCP-0052). Additionally, sincere thanks are extended to Dr Jagadeesh Babu Nanubolu, CSIR-Indian Institute of Chemical Technology, for his assistance in crystal studies (IICT Communication No. IICT/Pubs./2025/148).

## References

- 1 N. Harbeck, F. P. Llorca, J. Cortes, M. Gnant, N. Houssami, P. Poortmans, K. Ruddy, J. Tsang and F. Cardoso, *Nat. Rev. Dis. Primers*, 2019, **5**, 66.
- 2 F. Bray, J. Ferlay, I. Soerjomataram, R. L. Siegel, L. A. Torre and A. Jemal, *Ca-Cancer J. Clin.*, 2018, **68**, 394–424.
- 3 P. H. Lin and G. Laliotis, *J. Clin. Med.*, 2022, **11**, 5891.
- 4 D. Safarpour, A. Fattaneh and M. D. Tavassoli, *Arch. Pathol. Lab. Med.*, 2014, **139**, 612–617.
- 5 N. Affi and C. A. Barrero, *J. Clin. Med.*, 2023, **12**, 1375.
- 6 Z. Chen, Y. Liu, M. Lyu, C. H. Chan, M. Sun, X. Yang, S. Qiao, Z. Chen, S. Yu, M. Ren, A. Lu, G. Zhang, F. Li and Y. Yu, *Cell Biosci.*, 2025, **15**, 13.
- 7 N. Harbeck, F. Penault-Llorca, J. Cortes, M. Gnant, N. Houssami, P. Poortmans, K. Ruddy, J. Tsang and F. Cardoso, *Nat. Rev. Dis. Primers*, 2019, **5**, 66.
- 8 M. Nedeljković and A. Damjanović, *Cells*, 2019, **8**, 957.
- 9 R. Gopathi, M. P. Kumar, G. J. Kumar, N. P. Syamprasad, B. G. Kodiripaka, V. G. M. Naidu and B. N. Babu, *RSC Med. Chem.*, 2025, **16**, 1188–1198.
- 10 E. Marchesi, D. Perrone and M. L. Navacchia, *Pharmaceutics*, 2023, **15**, 2185.
- 11 N. Shagufta and I. Ahmad, *RSC Med. Chem.*, 2023, **14**, 218–238.
- 12 J. P. Soni, Y. Yeole and N. Shankaraiah, *RSC Med. Chem.*, 2021, **12**, 730–750.
- 13 M. Thatikayala, P. Wadhwa, P. Kaur, P. K. Singh, A. Yadav, M. Kaushik and S. K. Sahu, *Eur. J. Med. Chem. Rep.*, 2022, **6**, 100096.
- 14 R. Tokala, S. Sana, U. J. Lakshmi, P. Sankarana, D. K. Sigalapalli, N. Gadewal, J. Kode and N. Shankaraiah, *Bioorg. Chem.*, 2020, **105**, 104357.
- 15 B. Luo and X. Song, *Eur. J. Med. Chem.*, 2021, **224**, 113688.
- 16 T. T. Dang, N. T. T. Huyen, B. Van Phuc, T. T. Huyen, T. T. Hong, H. Nguyen, V. H. Nguyen, M. T. Nguyen, T. Q. Hung and C. P. Dinh, *ChemMedChem*, 2024, **19**, e202400316.
- 17 A. Kamal, M. Sathish, V. L. Nayak, V. Srinivasulu, B. Kavitha, Y. Tangella, D. Thummuri, C. Bagul, N. Shankaraiah and N. Nagesh, *Bioorg. Med. Chem.*, 2015, **23**, 5511–5526.
- 18 K. L. Manasa, S. Thatikonda, D. K. Sigalapalli, A. Sagar, G. Kiranmai, A. M. Kalle, M. Alvala, C. Godugu, N. Nagesh and B. N. Babu, *Bioorg. Chem.*, 2020, **101**, 103983.
- 19 Y. Tangella, K. L. Manasa, N. H. Krishna, B. Sridhar, A. Kamal and B. N. Babu, *Org. Lett.*, 2018, **20**, 3639–3642.



- 20 S. F. Duan, L. Song, H. Y. Guo, H. Deng, X. Huang, Q. K. Shen, Z. S. Quan and X. M. Yin, *RSC Med. Chem.*, 2023, **14**, 2535–2563.
- 21 A. Dorababu, *RSC Med. Chem.*, 2020, **11**, 1335–1353.
- 22 S. Kumar and N. Ritika, *Future J. Pharm. Sci.*, 2020, **6**, 121.
- 23 X. Mo, D. P. Rao, K. Kaur, R. Hassan, A. S. Abdel-Samea, S. M. Farhan, S. Bräse and H. Hashem, *Molecules*, 2024, **29**, 4770.
- 24 A. Banyal, S. Tiwari, A. Sharma, I. Chanana, S. K. S. Patel, S. Kulshrestha and P. Kumar, *3 Biotech*, 2023, **13**, 211.
- 25 R. Qin, F. M. You, Q. Zhao, X. Xie, C. Peng, G. Zhan and B. Han, *J. Hematol. Oncol.*, 2022, **15**, 133.
- 26 E. Russo, C. Grondona, C. Brullo, A. Spallarossa, C. Villa and B. Tasso, *Pharmaceutics*, 2023, **15**, 1815.
- 27 N. M. Saadan, W. U. Ahmed, A. A. Kadi, M. S. Al-Mutairi, R. I. A. Wabli and A. F. M. M. Rahman, *ACS Omega*, 2024, **9**, 41944–41967.
- 28 F. A. M. Mohamed, S. Y. M. Alakilli, E. F. E. Azab, F. A. M. Baawad, E. I. A. Shaaban, H. A. Alrub, O. Hendawy, H. A. M. Gomaa, A. G. Bakr, M. H. Abdelrahman, L. Trembleau, A. F. Mohammed and B. G. M. Youssif, *RSC Med. Chem.*, 2023, **14**, 734–744.
- 29 W. Zeng, C. Han, S. Mohammed, S. Li, Y. Song, F. Sun and Y. Du, *RSC Med. Chem.*, 2024, **15**, 788–808.
- 30 Y. Masuda, K. Asada, R. Satoh, K. Takada and J. Kitajima, *Phytomedicine*, 2015, **22**, 545–552.
- 31 L. Wang, H. Zhu, T. Peng and D. Yang, *Org. Biomol. Chem.*, 2021, **19**, 2110–2145.
- 32 P. N. P. Rao, Q. H. Chen and E. E. Knaus, *Bioorg. Med. Chem. Lett.*, 2005, **15**, 4842–4845.
- 33 A. K. Dhar, R. Mahesh, A. Jindal and S. Bhatt, *Arch. Pharm.*, 2015, **348**, 34–45.
- 34 L. Chen and C. J. Li, *Org. Lett.*, 2004, **6**, 3151–3153.
- 35 P. d. S. M. Pinheiro, L. S. Franco and C. A. M. Fraga, *Pharmaceutics*, 2023, **16**, 1157.
- 36 D. Aynetdinova, M. C. Callens, H. B. Hicks, C. Y. X. Poh, B. D. A. Shennan, A. M. Boyd, Z. H. Lim, J. A. Leitch and D. J. Dixon, *Chem. Soc. Rev.*, 2021, **50**, 5517–5563.
- 37 H. Schönherr and T. Cernak, *Angew. Chem., Int. Ed.*, 2013, **52**, 12256–12267.
- 38 L. Nocquet, J. Roul, C. C. Lefebvre, L. Duarte, M. Campone, P. P. Juin and F. Souazé, *Sci. Rep.*, 2024, **14**, 14177.
- 39 P. Quidute, R. Quidute, M. M. Perez, E. C. Pereira, G. L. Da Veiga, B. Da Costa Aguiar Alves and F. L. A. Fonseca, *Rev. Assoc. Med. Bras.*, 2023, **69**, e20230167.
- 40 A. Balaji, N. Udupa, M. R. Chamallamudi, V. Gupta and A. Rangarajan, *PLoS One*, 2016, **11**, e0155013.
- 41 T. Sarkar, M. Paul, A. Bera, A. A. Mandal, S. Banerjee, S. Biswas and B. N. Babu, *J. Med. Chem.*, 2025, **68**, 15137–15150.
- 42 S. Pulakkat, A. S. Balaji, A. M. Raichur and A. Rangarajan, *J. Drug Delivery Sci. Technol.*, 2025, **104**, 106494.
- 43 V. K. Jaina, A. Eedara, S. P. Svs, S. S. Jadav, S. Chilaka, R. Sistla and S. B. Andugulapati, *Process Biochem.*, 2022, **123**, 11–26.
- 44 J. S. Sawyer, D. W. Beight, K. S. Britt, B. D. Anderson, R. M. Campbell, T. Goodson, D. K. Herron, H. Y. Li, W. T. McMillen, N. Mort, S. Parsons, E. C. R. Smith, J. R. Wagner, L. Yan, F. Zhang and J. M. Yingling, *Bioorg. Med. Chem. Lett.*, 2004, **14**, 3581–3584.
- 45 T. A. Halgren, R. B. Murphy, R. A. Friesner, H. S. Beard, L. L. Frye, W. T. Pollard and J. L. Banks, *J. Med. Chem.*, 2004, **47**, 1750–1759.
- 46 S. Genheden and U. Ryde, *Expert Opin. Drug Discovery*, 2015, **10**, 449–461.
- 47 M. Pradeep Kumar, T. Sarkar, V. Durga Prasad, N. Sharma, K. B. Harish, A. Sai Balaji and B. Nagendra Babu, CCDC 2446994: Experimental Crystal Structure Determination, 2025, DOI: [10.5517/ccdc.csd.cc2n499f](https://doi.org/10.5517/ccdc.csd.cc2n499f).

